Proceedings of the Eighth Meeting of the International Collaboration on Advanced Neutron Sources (ICANS-VIII)
8-12 July 1985, Rutherford Appleton Laboratory Report RAL-85-110

TOF TYPE SMALL ANGLE SCATTERING SPECTROMETER SAN AT KENS PULSED COLD NEUTRON SOURCE

By Y. Ishikawa and M. Furusaka

Physics Department Tohoku University, Sendai 980 Japan

N. Niimura

Laboratory of Nuclear Science Tohoku University, Sendai 980 Japan

M. Arai

National Laboratory for High Energy Physics, Tsukuba, Ibaraki, 305 Japan

and K. Hasegawa

Department of Engineering, University of Tokyo, Tokyo 106 Japan

Abstract

The paper describes the configuration and performance of a new TOF type small angle neutron scattering spectrometer SAN installed at the pulsed cold neutron source in the National Laboratory for High Energy Physics(KEK). The spectrometer has a special advantage over the conventional small angle scattering machine in following two points. One is its ability for simultaneous measurements of wide Q range (3×10^{-3} $A^{-1} < Q < 4$ A^{-1}) and another is new information which it provides by employing the wavelength dependence of scattering. For example, the inelastic scattering can be separated from the elastic one without making energy analysis. The discussions have also been made on the design principle of this type of spectrometer.

§ 1. Introduction

The small angle neutron scattering spectrometer (SANS) is a special machine for investigating macro-structures and it becomes now one of the most important instruments for neutron scattering because of its application to wide scientific fields as solid state physics, chemistry, material sciences, polymer and biology.(Kosterez 1979) The demand for this machine is still increasing and therefore this machine is installed or at least planned to be installed in most of the research reactors in the world. The situation would be the same for the pulsed spallation neutron sources which are just coming out in the world as the next generation neutron sources, but because of its new feature; pulsed character, there was no agreement on the design principle of the TOF type SANS when we planned to install our small angle neutron scattering spectrometer "SAN" at the cold moderator of our spallation neutron source KENS in National Laboratory for High Energy Physics (KEK) (Ishikawa and Watanabe 1978). Only few papers had been published to report the results of preliminary tests of this type of spectrometers (Cser, 1975, Borso, 1981). Some people even suspected the installation of this machine to the spallation neutron source, partly because of small advantages of spallation neutron source (pulsed short wavelength neutrons) to this machine and the complexity of handling the 3 dimensional (3D) data (2D-position sensitive detector + TOF channels).

We have shown, however, by our four year's successful utilization, that the small angle neutron scattering spectrometer is also quite an appropriate spectrometer for the spallation neutron source, giving new information which is difficult to obtain with the conventional small angle scattering machine

installed at the reactor. The paper describes in the next section the overall layout and configuration of the spectrometer. Some instrumental devices newly developed for this spectrometer such as the two dimensional (2D)-converging Soller slit, which would also be useful for the conventional SANS, are also discussed in this section. Then the characteristics of the TOF-SANS are summarized in Section 3 with experimental results obtained with our spectrometer SAN. In the final section the design principle of the TOF-SANS is discussed in comparison with that of the conventional SANS in the steady reactor. The design principle of this spectrometer(SAN) as well as its scientific yields are reported in many short papers published in KENS Report I(1980)-V(1985) and in a review article (Ishikawa, 1983). The problems for data analysis of this spectrometer are discussed separately in a succeeding paper (Furusaka et al, 1985).

§2. Structure of SAN at KENS

2.1 Overall Layout

The layout of the SAN is displayed in Fig.1(a) and (b). The spectrometer is installed at the exit of a bent neutron guide from the KENS cold moderator with effective dimensions of h =10 cm, w = 8 cm, d = 5 cm made by solid methane at 20K (Ikeda et al., 1983). The distance between the source and sample is fixed to be ℓ_S = 19 m, where are located a 3.5 m long straight guide, a tail cutter C_1, a 11m long bent guide tube and a 2m long 2D-converging Soller slit. A 2D-position sensitive detector (PSD) (60 x 60 cm^2) is accommodated inside a large vacuum scattering chamber, 10^{-2} mmHg in pressure and the distance between

the sample to the detector ℓ_2 can be changed between 1 and 5 m without breaking vacuum. The SAN is also equipped with several normal ^{3}He counters noted as A, B, ..., F in the figure in order to expand the dynamical range of the Q measurements. The 2D-PSD consists of an array of 43 1D-PSD as described later in detail. The photograph of the SAN spectrometer as well as the 2D-PSD inside the vacuum chamber are shown in Fig.2. The tail cutter C_1 is designed to avoid the frame overlap of pulsed white neutrons operating with 20 Hz at the position of the detector, 25 m apart from the source. A range of wavelength [λ], which can be employed in the experiment is [λ] = 8 A and we usually use the neutrons with 3 A $\leq \lambda \leq$ 11 A. The range of momentum transfer Q covered with this wavelength band is displayed in Fig. 3 for four different 2D - PSD positions noted as G_1 - G_{10}(ℓ_2 = 1, 3, 5 and 10 m). The last position G_{10} is still in a stage of planning. The solid straight lines (A - F) are the ranges of Q covered with six single ^{3}He counters. From this figure, it is seen that the SAN with 2D - PSD at the position of 5 m can measure simultaneously a wide Q range between 3 x 10^{-3} A^{-1} and 4 A^{-1}.

2.2 Vacuum scattering chamber

In order to meet the requirement that the vacuum pressure of the large scattering chamber, 1.2 m in diameter, 6 m long, should be always 1 x 10^{-2} mm Hg, while that of the sample chamber can be varied between 10^{-6} mmHg and 1 atmospheric pressure depending on the experimental conditions, we put a specially designed vacuum shutter in between both chambers as shown in Fig. 4. The shutter valve in the open state is equipped with an immovable thin Al foil window, 0.3 mm thick and 200mm in diameter

which serves to keep two chambers in different vacuum states of 10^{-2} mmHg and 10^{-6} mmHg respectively. When we need to make the sample chamber to the atmospheric pressure for sample exchange or installation of other equipment as an electromagnet, a thick Al plate shutter with a 2mm thick Al window was closed behind the thin Al foil to support it against the atmospheric pressure. This device reduces significantly the time for changing the experimental conditions and saves the machine time.

Another convenient device we designed is a movable beam stopper in front of the 2D-PSD. It is preferable that the direct beam stopper can be removed for the transmission measurement or can be moved for centering. Therefore we put first a movable beam stopper which was hanged vertically by a rod of 10 mm wide and was driven electronically from outside in both horizontal and vertical directions. This system was, however, found not ideal because it reduces the detecting efficiency behind the hanging rod as shown in Fig. 5(a) where we demonstrate the scattering intensity from water detected by 2D-PSD. The time channels are integrated for simple demonstration. The beam stopper we finally adopted consists of a thin Al plate 0.4 mm thick covering the whole 2D - PSD with a small beam stopper(42 x 42 mm^2) made of Cd at the center of the plate which is shown in Fig. 6. The Al plate can be moved in the horizontal direction from outside. This system insured the homogeneity of the detecting efficiency as shown in Fig. 5(b).

2.3 2D-Converging Soller slit and background level of SAN

Although the principle of the 2D-converging Soller slit had been reported earlier(Nunes, 1978), no small angle neutron

scattering machines had hitherto adopted this slit, partly because of the difficulty of fabricating it and partly because of the anxiety for increasing the background level due to this slit. We designed a simple two dimensional converging Soller slit and found that the adoption of the slit is particularly important for the TOF type small angle neutron scattering machine.

The principle of the converging Soller slit is displayed in Fig. 7. This is the Soller slit system which collimates the incident neutrons so as to converge them into the center of the 2D-PSD. Therefore the scattering angle ϕ of the neutrons scattered from any sample position is conserved even if we use the large sample ($\phi = \phi_o$ in Fig. 7(a)). The layout of the 2D converging Soller slit finally we designed is shown in Fig. 8. The slit consists of two sets of one dimensional converging Soller slits, each making the neutrons converge in horizontal and vertical directions respectively. The slit is made of Gd_2O_3 coated thin iron plates, 0.2 mm thick. The results of using the 2D converging Soller slit is displayed in Fig. 9, where the incident neutron beam divergences at the position of 5 m from the sample are displayed as the contour maps of equal intensity for three different wavelengths. The lower curves correspond to the case without the slit, while the upper one is the result of insertion of the slit. We can see in the lower figure that without collimation (i) the divergence of the beams is larger for longer wavelength corresponding to the larger critical angle $\theta_c(\lambda)$ of the neutron guide and (ii) the beam intensity is shifted to the left hand side for 4 A because of existence of garland type reflections inside the guide for this wavelength. Note that the concavity of the intensity map at the left hand side is due to

the presence of the beam stopper. Such a difference in the divergence as well as the inhomogenous intensity distribution for different wavelengths are completely disappeared, when we use the Soller slit as shown in the upper figures. Since the spacial homogeneity of the intensity is usually achieved by connecting a long straight guide to the bent guide, we found that the converging Soller slit is particularly useful for the TOF machine which requires a shorter flight path than the conventional SANS.

The effect of the background by this collimator was examined as shown in Fig.10, where the background under four different conditions are compared with the scattering from a standard sample, SiC powder. The background marked as Al window is the case where the sample case has two Al windows, 0.5 mm thick, while in case of Si(Single), the windows are replaced by single crystal Si plates, 3 mm thick.(See also Fig. 4). In the latter case, the background level was found to be reduced almost to the real background (BG) which corresponds to the case of no window. The background is of course three order of magnitude smaller than the signal intensity for small Q values. The background at high Q values was also compared with the scattering from pure water, 2 mm thick in Fig. 11, which indicates that the S/N ratio is about 100 for $Q > 0.02\ A^{-1}$, sufficiently high for the study of solution, but the background starts to increase below this Q value. The increase of background is partly due to a small leakage of the direct beam and presumably partly to the small angle scattering from the Soller collimator. Although the S/N ratio in this Q range reduces less than 1/5 for water, the situation is much improved for the actual small angle scattering because of the increase of signal intensity at small Q side.

Total neutron intensity is about 10^6 of the background at $Q = 0.01\ A^{-1}$. Note that the 2D-PSD has no shield and the scattering chamber is shielded only by a Cd sheet, 0.5 mm thick.

The incident beam collimation realized by the converging Soller slit is quite important, because it determines the final resolution of the spectrometer as will be discussed in Section 4.3, all other resolutions can be matched to this resolution. Referring to Fig. 7(a), the angular resolution of the converging Soller slit is given by

$$\Delta\phi^2 = \frac{1}{2}\left[\left(\frac{2d_o}{\ell_1}\right)^2 + \left(2d_1 \cdot \left(\frac{1}{\ell_1} + \frac{1}{\ell_2}\right)\right)^2 + \left(\frac{2d_2}{\ell_2}\right)^2\right]^2 , \qquad (1)$$

where $2d_o$, $2d_1$, and $2d_2$ are respectively the slit widths at the positions of entrance of the collimator, and that in front of sample and detector. The characteristic feature of the converging Soller slit is that $\Delta\phi$ does not depend on R_o or R_s, the positions of the incident beam on the collimator or sample. If the beam convergence is ideally realized (Fig. 7(a)),

$$2d_o/\ell_1 = 2d_1 \quad (1/\ell_1 + 1/\ell_2) \qquad (2)$$

This relation also corresponds to the resolution matching. Therefore

$$\Delta\phi^2 = \frac{1}{2}\cdot\left[2\left(\frac{2d_0}{\ell_1}\right)^2 + \left(\frac{2d_2}{\ell_2}\right)^2\right] = \Delta\theta^2_{col} + \Delta\theta^2_{det} . \qquad (3)$$

The momentum resolution $\Delta Q/Q$ is then given by

$$\left(\frac{\Delta Q}{Q}\right)^2 = \left(\frac{\Delta\lambda}{\lambda}\right)^2 + \left(\frac{\Delta\phi}{\phi}\right)^2 . \qquad (4)$$

Since $\Delta\lambda$ = 0.25A for SAN, $(\Delta\lambda/\lambda)^2$ ($<<$ 0.01) can be practically neglected in (4). The minimum 2D - PSD resolution being about $\pm$5 mm and $\Delta\theta_{det}^2 \simeq 1/2(1/500)^2 = 2 \times 10^{-6}$ for ℓ_2 = 5m. Therefore

$$\frac{\Delta Q}{Q} \cong \frac{\Delta\theta_{col}}{\phi} \quad \text{or} \quad \Delta Q \cong \Delta\theta_{col} \frac{2\pi}{\lambda} \ . \tag{5}$$

Our convergning Soller slit having an angular divergene $\Delta\theta_{col} = 2.9 \times 10^{-3}$, $\Delta Q_{min} = 1.65 \times 10^{-3}$ A^{-1} for λ = 11A, which is about 1/2 of Q_{min} ($= 3 \times 10^{-3}$ A^{-1}) of our spectrometer.

In case of 3 m scattering; ℓ_2 = 3 m, we use a half set of our converging Soller slit, one pair of vertical and horizontal collimators, each being 50 cm long. $\Delta\theta_{col}$ then becomes 5.8×10^{-3}. This configuration, however, breaks the condition of beam convergence (Fig. 7(b)), resulting in adding another term $\Delta\theta^2_{nc}$ in Eq(3). A simple geometrical calculation shows that $\Delta\theta^2_{nc}$ is given by (Ishikawa et al 1980)

$$\Delta\theta^2_{nc} = \frac{1}{2} \left(\frac{R_s}{\ell_2^0} \frac{\Delta\ell}{\ell_2}\right)^2 \ , \tag{6}$$

with notations defined in Fig. 7(b). By putting R_s = 18 mm, ℓ^o_2 = 5 m, ℓ_2 = 3 m, $\Delta\ell$ = 2 m, to Eq(6), $\Delta\theta_{nc}^2 = 2.9 \times 10^{-6}$ is obtained, which is much smaller than $\Delta\theta^2_{col} = 3.4 \times 10^{-5}$. Therefore the converging Soller slit given in Fig. 8 can be used for both 5 m and 3 m scattering measurements. The latter configuration increases the intensity of incident neutrons by a factor four compared with the 5 m scattering and can cover the momentum transfer higher than 0.01 A^{-1}. For the 1 m scattering, we use only a vertical convergning Soller slit with appropriate dimension.

2.4 Detector system

The 2D-PSD we adopted consists of an array of 43 x 1 D - PSDs, 1/2" in diameter and 24" in active length with 6 atom ^{3}He originally developed at Missouri University (Berlinger et al. 1981) (Reuter - Stokes). This is the charge sensitive PSD with low resistive anode wire (3.6kΩ), particularly suitable for the TOF measurement because of rapid time response. Since the 2D - PSD with a bank of 90 preamplifiers is accommodated inside a vacuum scattering chamber with a typical operating pressure of < 1.5×10^{-2} mmHg, a voltage as high as 1900 V can be safely applied to each 1D - PSD, enabling a position resolution of 7 mm to be achieved. We could not apply more than 1 kV in atmospheric pressure because of high humidity in Japan.

A block diagram of the data processing system for the 2D - PSD is shown in Fig. 12. The neutron event position is calculated by charge division method. The position is determined by the following expression

$$X = \frac{Q_A}{Q_A + Q_B} \quad , \tag{7}$$

where Q_A and Q_B are the charges detected at each end of a 1D - PSD. Charge sensitive preamplifiers convert Q_A and Q_B to voltage signal, directed to the main amplifiers and its outputs are summed and fed to a single channel pulse height analyzer (Discriminator). When the sum of Q_A and Q_B is within a preset limit, a standard set signal is generated, which is used as a gate signal for the sample & holder circuit, analogue to digital converter (ADC) and time analyzer. Since the conversion speed of the ADC is prompt (5μ sec), a single ADC

can handle the signals from 4 different detectors. The digitized values of Q_A and $Q_A + Q_B$ are transferred to the address register of the P-ROM, where the positions calculated according to the expression (7) are tabulated. The operation time for calculation of the position is reduced to be 1 μ sec - access time of P-ROM by this table. The discriminator output is used to determine the neutron time of flight. Finally the data corresponding to the position, detector number and time of flight creates one address and add-one process is performed to this address of a bulk memory.

The advantages of adopting the array of 1D - PSDs for the TOF-2D-PSD are summarized below.

(i) The interference between X and Y directions can be avoided absolutely.

(ii) Some troubles of a single detector never result in a fatal wound. This is particularly true for the TOF measurement because the same information can be obtained from different detectors by employing different wavelengths.

(iii) The total dead time of the detector can be reduced (50 μ sec in our system).

We encountered little troubles of 2D-PSD during four years operation.

§ 3. Characteristics of TOF type SANS

- experimental results obtained with SAN -

3.1 Simultaneous measurements of wide Q range

The most important characteristic of SAN is its potential for measuring simultaneously a wide range of momentum transfers as shown in Fig. 3. Such a wide dynamical range of measurements

is indispensable when we study nonequilibrium phenomena as phase separation process (Furusaka et al 1983). One typical example of the results obtained with SAN is displayed in Fig.13, where we plot the temporal variation of the scattering function $I(q,t,T_a)$ of an $Fe_{60}Cr_{40}$ alloy in a process of phase separation when the sample is annealed at T_a = 550 C for annealing time t. Note that simultaneous measurements of nearly two order of magnitudes of momentum transfers ($0.02 \lesssim Q \lesssim 0.6$ A^{-1}) are required to get the complete profiles of the scattering functions of I(Q,t,Ta) in the whole decomposition process, which is impossible to practice with the conventional SANS employing a monochromatized beam as indicated by a line in a lower part of the figure. We have shown in a previous paper (Furusaka et al, 1985) that the measurements of the tail part of the scattering function are quite important to distinguish the early stage of decomposition from the late stage. In the latter stage the scattering function obeys the Q^{-4} law for large Q and the scaling law holds, while in the early stage the tail part obeys the Q^{-2} law and the scattering function cannot be scaled in a similar way.

Another typical example of the simultaneous measurement of wide Q range is provided by the study of the magnetization process in a single crystal of $90FeTiO_3$-$10Fe_2O_3$, a typical cluster type spin glass (Arai et al 1985 a, b). In this study, in addition to the small angle scattering detected by 2D - PSD, the magnetic scattering around the (1,0,1) and (1,0,-0.5) reciprocal lattice points was measured simultaneously with two ^3He counters placed at high angles as shown in Fig. 14. The (1,0,1) scattering is equivalent to the (0,0,0) scattering and they give an information on the ferromagnetic short range correlations,

while the (1,0,-0.5) scattering suggests the presence of amplitude modulation of the ferromagnetic correlations inside the short range order. The scattering patterns around three different Bragg points are displayed in Figs.14(a), (b) and (c). We have studied the effect of the magnetic field on the scattering around these three reciprocal lattice points (Arai et al, 1985 b) and found that no change occurs in the magnetic structure inside the short range order if the magnetic field is less than 5 kOe. Such simultaneous measurements of small angle scattering and Bragg reflections are quite important for the study of the irreversible process, but cannot be realized with the conventional SANS.

3.3 Studies of small angle Bragg scattering with single crystals

The TOF type small angle scattering machine is particularly suitable for the study on the single crystal, as described in the previous section. In case of small angle Bragg scattering with SAN, the same Bragg reflections around (0,0,0) are detected by different wavelengths at many different positions on the 2D - PSD. A typical example of measurements is provided by the scattering from a single crystal of MnSi which is known to have a helical spin structure with a long period of 180 A along <111> below T_N = 29.5 K.(Ishikawa et al, 1976) Therefore four satellites appear at $\langle q_s, q_s, q_s \rangle$ with q_s = 0.035 A^{-1} as shown in Fig. 15, but in many different positions on the 2D - PSD for different wavelengths. The value of q_s determined with different λ is plotted against λ in Fig. 16(a), which indicates that q_s does not vary with λ. This is the best way to check the accuracy of the position determination of 2D - PSD and the result

indicates it satisfactory. Thus $q_s = 0.035 \pm 0.005$ A^{-1} is determined at 13 K (Ishikawa et al, 1984), in good agreement with a previous measurement with D 11 spectrometer at ILL (Ishikawa et al, 1976). Fig. 16(b) is plotted the intensity of the satellite reflections as a function of λ. The λ dependence of the satellite intensity can be understood, if we consider that the simultaneous detection of four satellites in the (1,1,0) reciprocal plane with the 2D - PSD placed perpendicular to the incident beam is a result of the finite size of the satellites as shown in Fig. 17(a); the Ewald sphere can cross with the satellites even if it does not cross the (1,1,0) plane. Thus the gradual decrease of intensity of the satellites with increasing λ is due to the decrease of overlapping area because of the decrease of the radius of the Ewald sphere. The size of the satellites can be determined directly from the rocking curve which is obtained by rotating the sample around the vertical axis. The rocking curve thus obtained has a FWHM of 2.57 degs as shown in Fig. 17(b), which corresponds to the momentum spread Δq_B of 1.57×10^{-3} A^{-1}. The helical spin structure of MnSi has therefore a coherent length $\xi = 2\pi / \Delta q_B = 4000$ A. The λ dependence of the intensity of satellites can be calculated by using this satellite size and the result of calculation is plotted by a broken line in Fig. 16(b). The agreement between observation and calculation is quite satisfactory, indicating that the satellite size can be determined automatically from the λ dependence of the intensity without rotating the crystal. In Fig.16(c) are plotted the width of satellite $(\Delta q/q)^2$ plotted against $1/\lambda^2$. The solid line is calculated by (22) which takes into account the instrumental resolution as will be discussed later. The agreement

between the observation and calculation is again satisfactory, indicating that the instrumental resolution can accurately be taken into account for SAN. The extrapolation of $\Delta q/q$ to $1/\lambda^2 = 0$ gives in principle the resolution free momentum spread Δq_B, but the previous method (Fig. 16(b)) can make a better determination. Thus a single measurement of Bragg reflections with our SAN provides much more information than that obtained with the conventional SANS.

3.4 Separation of inelastic scattering with a chopper

One of the important problems for small angle scattering is to distinguish the scattering due to the heterogeneity (static origin) from inelastic scattering as magnon scattering. This can in principle be performed by chopping the incident neutrons in front of the sample and by measuring the TOF spectra of the scattered neutrons. Since, however, it looses significantly the neutrons to be used in the experiment and increases the size of data memory bank by one order of magnitude, only few experiments have ever practiced the separation of the inelastic scattering.

Our spectrometer is quite suitable for this purpose. It is enough for us to put a chopper(C_2 in Fig.1(a)) in front of the sample. Our SAN is equipped with two different types of choppers for different purposes. One is a chopper with many windows (Fig. 18(a)) to modulate in time (wavelength) the incident neutrons and another has only one windows (Fig. 18(c)) to monochromatize incident neutrons, both are operated with a frequency of 80 Hz synchronizing with the neutron pulse(20 Hz). The former is used to reject the inelastic part, while the latter for measuring the inelastic scattering as schematically shown in Fig. 18(b) and

(d). One example of the test experiments with the first type chopper is shown in Fig. 19, where the time spectra measured with three different detectors are demonstrated. The upper two figure are the spectra obtained with a fixed counter at the position of 150 degs scattering while the lower two are those with different 1D - PSD by disregarding the positional information to increase the counting rate. The lowest pattern obtained with 22th 1D-PSD shows the time modulation of incident neutrons, thus it corresponds to the pattern of elastic scattering. Except this case, the modulated spectra do not go to zero because of presence of the inelastic part, suggesting that the inelasticity is involved in the scattering. The elastic part can be separated by deconvoluting the modulated part. The energy resolution of the spectrometer with 2D - PSD at 3 m from the sample is about o.6 meV for 4 A. Although the measurement is still in a stage of preliminary test, the method will be applied successfully in some practical problems.

3.5 Separation of magnon scattering without chopper

We have also found that the inelastic scattering as magnon scattering can be separated from the small angle scattering of static origin simply by analyzing the dependence of the scattering functions. The principle is that, in case of elastic scattering, the scattering function is independent of the wavelength of incident neutrons, which is not the case if the inelasticity is involved in the scattering. In case of magnon scattering with a momentum and an energy transfers of q and h_m respectively, the scattered neutron wave vector k_f varies from the incident neutron wave vector k_i as

$$\frac{h^2 k_i^2}{2m} - \frac{h^2 k_f^2}{2m} = \pm \hbar\omega_m \,, \tag{8}$$

$$k_i - k_f = \pm q.$$

Since $\hbar\omega_m = Dq^2$, a simple calculation shows that the scattering occurs within the critical angle ϕ_c given by (Hatherly et al, 1964)

$$\phi_c \cong \frac{\hbar^2}{2m} \frac{1}{D} \,, \tag{9}$$

which is independent of the incident neutron wavelengths. In Fig. 20(a), we plot the small angle scattering from Fe_3Pt for different wavelengths separately against Q, which shows clearly that the scattering at high Q side has a dispersion for different wavelengths, but if we plot the scattering intensity multiplied by k_i^2 against scattering angle θ (Fig.20(b)), all the scattering for different wavelengths fall on a single line suggesting that the small angle scattering at high Q side is due to the magnon scattering. Thus the measurement of the wavelength dependence of the scattering function gives an information on the existence of inelastic scattering and in case of magnon scattering we can separate its contribution from the small angle scattering of other origins, which is difficult to practice with the conventional small angle scattering machine. In this way, we successfully measured the small angle scattering of static origin in Fe_3Pt and the results as well as the detailed method for analysis will be published separately.

3.6 Real Time Spectroscopy

By real time spectroscopy, we mean the measurement of the slow relaxation phenomena with a relaxation time of order of 10^{-3}~1 sec, where the external condition as magnetic field or temperature is varied abruptly and the change of positional correlations which follows is measured in real time. Though this technique can also be applied to the conventional small angle scattering machine at the continuous reactor, the TOF type SANS is more effective than this because of the simultaneous measurement of wide Q range. In order to make the real time spectroscopy possible, the KENS-SAN is equipped with a large external memory bank of 2 M bites so as to make possible the collection of data in eight different conditions sequentially as shown in Fig. 21 which show a preliminary result of measurements of variation of the spin glass state under a pulsed magnetic field. The squared pulsed field of 5 kOe was applied in a certain time interval with a rise time of 10 m sec and the variation of the spin correlations in a typical cluster type spin glass of $0.9FeTiO_3$-$0.1Fe_2O_3$ was observed in a time interval of 50 m sec.

This experiment was realized by employing a micro-processor LSI 11/23 and a bulk memory bank of 2M bites. The schematic diagram of the SAN's data acquisition system for this purpose is shown in Fig. 22. The pulsed magnetic field is applied synchronizing with the neutron source and the 2D -PSD data giving the temporal variation of the spacial correlations were sent successively to eight different memory area in the external bulk memory by the control of the μ processor. The system is particularly suitable for studying the nonequilibrium phenomena with relaxation time more than 50 msec. The detailed result of

the relaxation phenomena in the spin glass system will be published in a separate paper.

§4 Design Principle

The design principle of the TOF type small angle neutron scattering spectrometer installed at the pulsed neutron source should be somewhat different from the conventional one because of employing a band of wavelengths. In this section we will discuss this problem based on our experience.

4.1 Neutron Source

The intensity of scattered neutrons with wavelength between λ and $\lambda + \Delta\lambda$, from a sample with cross section , $I(\lambda)\Delta\lambda$ is given in general by

$$I(\lambda)\Delta\lambda = i(\lambda)\Delta\Omega_i \frac{d\sigma}{d\Omega}(\phi) S \Delta\Omega_d \eta_s \eta_d \Delta\lambda \ , \tag{10}$$

where $i(\lambda)\Delta\lambda$ is the intensity of incident neutrons with λ between λ and $\lambda + \Delta\lambda$ and is given by

$$i(\lambda) = \frac{\lambda_T^4}{\lambda^5} \exp(-\lambda_T^2/\lambda^2) \ . \tag{11}$$

λ_T is the characteristic wavelength of the moderator at temperature T defined by

$$\lambda_T = h/\sqrt{2mkT} \ . \tag{12}$$

$\Delta\Omega_i$, and $\Delta\Omega_d$ are the solid angles of initial and final beams respectively. $\Delta\Omega_i$ is given by squares of $\Delta\theta$: angular resolution of the incident beam. If we define the momentum resolution ΔQ, by the request of the measurement, $\Delta\theta$ depends on λ and is given

by

$$\Delta\theta = \frac{\lambda}{2\pi}\Delta Q \ , \tag{13}$$

while in the 2D-PSD, $\Delta\Omega_d$ can be determined so as to satisfy the relation

$$\frac{d\sigma}{d\Omega}(\phi)\ \Delta\Omega_d = \frac{d\sigma}{d\Omega_Q}(Q)\Delta Q^2 \ , \tag{14}$$

independent of λ. $d\Omega_Q$ being the solid angle in the Q space, η_s is the scattering efficiency at the sample and may be proportional to $1/\lambda$, if the neutron absorption by the sample obeying the 1/v law. The detecting efficiency η_d can be assumed as 1 for cold neutrons. $\Delta\lambda$ is determined by the TOF time channel width Δt_c and can be selected to satisfy.

$$\frac{\Delta\lambda}{\lambda} = \frac{\Delta t_c}{t} \cong \frac{\Delta Q}{Q} \ . \tag{15}$$

If $\Delta Q/Q$ is selected to be 0.1, Δt_c can be much longer than the neutron pulsed with Δt_m which is about 150μ sec for λ = 6 A, t, total flight time being an order of 30 msec.

Finally by assuming that $d\sigma/d\Omega_Q$ is independent of λ, the λ dependence of the scattered neutrons $I(\lambda)$ in Eq(10) is reduced to be

$$I(\lambda) = \frac{\lambda_T^4}{\lambda^4} e^{-\lambda_T^2/\lambda^2} C(\Delta Q)^4 \ . \tag{16}$$

The optimal wavelength λ_{opt} giving the maximum intensity is therefore given from $dI/d\lambda = 0$ to be

$$\lambda_{opt} = \frac{1}{2^{1/4}} \lambda_T \cong 0.84 \lambda_T \cdot \quad (17)$$

The incident neutron collimation $\Delta\theta_{col}$ is determined as

$$\Delta\theta_{col} = 2 \cdot \frac{\lambda_{opt}}{2\pi} (\Delta Q)_{min} , \quad (18)$$

since ΔQ_{min} is usually determined referring to the smallest Q value. The total scattered neutron intensity $I_T(\lambda_T)$ in case of employing the incident neutrons with λ between λ_{min} and λ_{max} is given by

$$I_T(\lambda_T) = C \int_{\lambda_{min}}^{\lambda_{max}} I(\lambda) d\lambda \cong C \lambda_T^4 \int_0^{\infty} \frac{1}{\lambda^4} \exp(-\lambda_T^2/\lambda^2) d\lambda = C\sqrt{\pi} \lambda_T . \quad (19)$$

The result indicates that even in case of the TOF type small angle scattering machine which utilizes all wavelengths, it is preferable to use the cold neutron source. Note that the peak intensity is higher for the normal moderator than the cold moderator as shown in Fig. 23 where the neutron spectra from the KENS normal moderator (polyethylene plate at 295 K) and cold moderator (solid CH_4 at 20 K) are compared in a normalized scale.

Note also that, in case of small angle scattering machine at the steady state reactor, the employment of the cold neutrons is indispensable to avoid the multiple Bragg scattering, but the TOF small angle scattering machine inevitably uses the shorter wavelength than the Bragg cut off in order to expand the dynamical range of measurements. The effect of multiple Bragg scattering can be estimated because of making the same measurement with longer wavelengh. Therefore the neutron source spectra should

have good intensities for both of shorter (λ < 4 A) and longer wavelengths. The cold moderator is better than thermal one to satisfy this condition.

4.2 Neutron Guide

In case of the continuous reactor, it is preferable that the SANS is installed at the exit of the bent neutron guide, because it significantly reduces the background. This principle is not necessarily applicable to the TOF-SANS with the pulsed neutron source because the background due to the high energy neutrons can automatically be separated from the signal by time channels. The first merit of using the guide tube is to conserve the beam divergence in long distance. The situation is demonstrated in Fig.24. If we don't use the neutron guide, the beam divergence $(\Delta\theta)^2$ is determined by the solid angle $(\Delta\theta_m)^2$ which the cold moderator spans to the sample;

$$(\Delta\theta_m)^2 = \frac{h \cdot w}{\ell_s^2} \quad . \tag{20}$$

In case of KENS cold moderator with h_{eff} = 10 cm and w_{eff} = 8 cm, the solid angles for ℓ_s = 9 m is given by 98.8 $(mrad)^2$ and for ℓ_s = 19 m, 4.8 $(mrad)^2$ assuming the cross section of flight path to be 3 cm^w x 5 cm^h, independent of λ . If the neutron guide with Ni coated mirror is employed, the critical angle $\theta_c(\lambda)$ being given by

$$\theta_c(\lambda) = 1.73 \times 10^{-3}\lambda \ (A) \quad . \tag{21}$$

The beam divergence is then determined by the collimator $\Delta\theta_{col}$ for longer wavelength and for λ for which $\theta_c(\lambda) < \Delta\theta_{col}$, the

divergence follows a $\theta_c(\lambda)$ line in Fig. 24 and for $\theta_c(\lambda) < \Delta\theta_m$, the divergence becomes equal to the direct glancing angle $\Delta\theta_m$, independent of λ. In case of the bent guide tube with cut off wave length λ_c (4 A in case of KENS), there is a steep decrease of intensity of neutrons with λ less than λ_c as shown by solid lines in Fig. 24. The difference in total intensity on the sample in three cases of without guide (NG), with straight guide (SG) and bent guide at the positions of 9 m and 19 m are more clearly seen in Fig. 25, where the energy spectra of these three cases are plotted against λ. We can see clearly that the neutron guide significantly increases the neutron total intensity and the gain in the intensity for the straight guide against the bent guide in the short wavelength region becomes also more significant for shorter ℓ_s. Therefore if the fast neutrons contribution to the background is not important, it is better to install the SANS spectrometer as close as possible to the source by using the straight guide. In KENS we finally adopted the bent guide because of the unknown factor for the background coming from fast neutrons. This choice was found successful and we have encountered no troubles for the background even if the 2D - PSD has no shield as described in the previous section. If the emphasis is put on the lower Q measurements, our choice would be still correct, because no difference in the intensity appears for longer λ which is important for low Q measurements.

4.3 Resolution

In the TOF-SANS, it is better to define the resolution not by $\Delta Q/Q$, but by ΔQ, because the incident neutron collimation $\Delta\theta_{col}$ being fixed, the incident neutron resolution $\Delta Q/Q$ varies

with λ. The total momentum transfer resolution ΔQ is given by

$$\Delta Q^2 = \left(\frac{\Delta\lambda}{\lambda}\right)^2 Q^2 + \left(\frac{\Delta\phi}{\phi}\right)^2 Q^2 + \Delta Q_{anal}{}^2$$
$$= \left(\frac{2\pi}{\lambda^2}\phi\right)^2 \Delta\lambda^2 + \left(\frac{2\pi}{\lambda}\right)\cdot(\Delta\theta^2{}_{col} + \Delta\theta^2{}_{det}) + \Delta Q_{anal}{}^2 , \quad (22)$$

where the last term $\Delta Q^2{}_{anal}$ is the momentum resolution introduced in a process of data analysis. Since $\Delta\lambda$ (time resolution) and $\Delta\theta_{det}$ (positional resolution on 2D-PSD) as well as ΔQ_{anal} should be chosen so as to match to $\Delta\theta_{col}$ in data analysis, it is better to select the original time and PSD channel widths as small as possible. Eq(22) shows that for a given ΔQ^2, $(\Delta Q/Q)^2$ varies with as $1/\lambda^2$ as actually found in the measurement of Bragg reflections (Fig. 16c). Note that the slope of the solid line in this figure is determined not by $\Delta\theta_{det}$ by ΔQ_{anal}.

§5. Conclusion

The TOF type small angle scattering machine SAN we have installed at KENS cold neutron source has been proved to be a unique and useful machine, having provided many interesting results in many fields of sciences in this four years. Note that the cold neutron source of KENS is very small; it is cooled by a small refrigerator of 40 W (15 K). The machine is particularly powerful for the study of nonequilibrium phenomena because of its unique ability for the wide Q measurements. The separation of inelastiac scattering will be another promising aspect of this spectrometer. We should also remark that the machine was also found to give good results for the studies of polymer (Okano et al, 1983) and biological materials (Hirai, 1985) in solution. One reason is that the contrast matching of solvent can

accurately be realized by measuring the λ dependent transmission (Hirai et al, 1985). We believe that the utility of this type of SANS will be increased more by further studies.

Although we have thus found that our SAN is quite satisfactory, we suggest that the installation of SAN directly to the straight guide from the cold neutron source would give a better performance, which we would like to test one day. Finally we should also remark that the TOF-SANS should be installed as close as possible to the source to avoid the frame overlapping problem and the improvement of the positional resolution of 2D-PSD is indispensable for it.

Acknowledgement

The authors would thank H. Sasaki, N. Watanabe and Y. Endoh for their interests and encouragements. Their thanks are also due to S. Ikeda for his assistance in construction in the early stage and to all members of the SAN's machine group, particularly to K. Kurita, S. Yamaguchi, Y. Fujino and M. Hirai for their collaborations in the measurements.

References

Arai, M., Ishikawa, Y., Saito, N. & Takei, H. (1985 a)
J. Phys. Soc. Jpn 54 781 - 794.

Arai, M. & Ishikawa, Y. (1985 b)
J. Phys. Soc. Jpn 54 795 -802.

Berlinger, R., Mildier, D.F.R., Pringle, O.A. & King, J.S. (1985)
Nucl Instru. Meth. 185 481 - 495.

Borso, C.S., Carpenter, J., Williamson, F.S., Holmblad, G.L.
Muller, H., Faber, J.Jr., Epperson, J.E. & Danyluk, S.S.(1982)
J. Appl. Cryst. 15, 443 - 448.

Cer L. (1975), Neutron Scattering for the Analysis of Biological
Structures pp. V113 - V1129. BNL Report - 50453, BNL, New
York, USA.

Furusaka, M., Ishikawa, Y., Yamaguchi, S & Fujino, Y. (1983)
Physica 120B 383 - 386.

Furusaka, M., Ishikawa, Y. & Mera, M. (1985 a)
Phys. Rev. Letts 17 2611.

Furusaka, M., Arai M. & Ishikawa, Y. (1985 b)
J. Appl. Cryst. succeeding paper.

Hatherly, M., Hirakawa, K., Lowde, R.D., Malett, J.F.,
Stringfellow, M.W. & Torrie B.H. (1964)
Proc. Phys. Soc. 84 55 - 62.

Hirai M. (1985), Neutron Small Angle Scattering Study of
Nucleosome Core, ph. D. Thesis Tohoku Univ.

Ikeda, S., Ishikawa, Y. and Inoue, K. (1981)
Proc ICANS- IV, KENS Report II, 200 - 209, KEK, Tsukuba,
Japan.

Ishikawa, Y., Tajima, K., Bloch, D. & Roth, M. (1976)

Solid State Commu. 19 525 - 528.

Ishikawa, Y., Furusaka, M., Arai, M., Niimura, N., Ikeda, S. & Hasegawa, K. (1980), KENS Report 1, 101 - 126, KEK, Tsukuba, Japan.

Ishikawa, Y. (1983), Physica 120 B 3 - 14.

Ishikawa, Y. & Arai, M. (1984) J. Phys. Soc. Jpn 53 2726 - 2733.

Kosterez, G. (1979) Treatise on Materials Science and Technology Vol 15, Neutron Scattering, ed. by Kostorz, G. pp 227 - 289, Acad. Press. London, UK.

Okano, K., Kurita, K. Nakajima, S. Wada, E., Furusaka, M. & Ishikawa, Y. (1983) Physica 120 B 413 - 417.

Figure Captions

Fig. 1 Layout of KENS SAN (a) overall arrangement and (b) around sample and detector chambers.

Fig. 2 (a) Photograph of SAN's vacuum scattering chamber and (b) 2D position sensitive detector installed inside the vacuum chamber.

Fig. 3 Ranges of wave vector Q measured with SAN. Solid lines are ranges covered by single counters, while broken lines are those by 2D-PSD installed at four different positions.

Fig. 4 SAN's vacuum scattering chamber with a special vacuum shutter to separate the sample chamber from the detector chamber.

Fig. 5 Scattering intensities from water detected by 2D-PSD in cases of (a) employing a movable beam stopper hung from the top and (b) adopting a new beam stopper described in the text.

Fig. 6 (a) A new movable beam stopper system composed of a large thin Al plate of 0.4 mm with a Cd beam stopper at the center. The Al plate can be moved horizontally by an electric device. (b)its photograph.

Fig. 7 Principle of converging Soller collimator system (a) in converging condition and (b) in non converging condition.

Fig. 8 SAN's converging Soller slits designed for 5 m 2D-PSD.

Fig. 9 Direct beam profiles without Soller(lower figures) and with (upper figures) converging Soller collimators.

Fig. 10 Comparison of backgrounds with signals from SiC sample

detected by 5 m 2D-PSD in case of with only thin Al windows, Si single crystal windows and without any window materials (BG).

Fig. 11 Comparison of background with signal from water detected by 5 m 2D-PSD.

Fig. 12 Block diagram of data processing system for TOF-2D-PSD.

Fig. 13 Temporal variation of scattering functions measured with SAN for $Fe_{60}Cr_{40}$ at room temperature in a process of phase separation ,when the sample was annealed at T_a = 550 C. (Furusaka et al. 1983).

Fig. 14 Simultaneous measurements of (a)small angle scattering and (b) and (c) Bragg reflections from a single crystal of $90FeTiO_3$-$10Fe_2O_3$ which exhibits a typical characteristics of cluster type spin glass. (Arai et al 1985 a) Detector configuration is shown on the reciprocal lattice plane in a upper left part of the figure.

Fig. 15 Four satellite reflections from MnSi at 15 K around (0,0,0) in the (0,1,1) reciprocal plane. The satellites along [1 0 0] and [0 1 1] would be multiple reflections.

Fig. 16 (a) Wavelength dependence of satellites position q_s, (b)integrated intensity of satellites I, and (c)linewidth of satellites $\Delta q/q$. A broken line in (b) and solid line in (c) are calculated (see text).

Fig. 17 Observation of satellites in the (0,1,1) plane by neutrons with different wavelengths impinging perpendicular to the plane. (a) Ewald spheres and satellites with finite sizes. (b) Rocking curve (open circles) of a satellite obtained with a single wavelength by rota-

ting the crystal around a vertical axis.

Fig. 18 Second chopper C_2(Fig. 1) for inelastic scattering. (1) chopper for rejecting inelastic scattering and (2) chopper for measuring inelastic scattering.

Fig. 19 Time modulation of small angle scattering from Fe_3Pt at room temperature when a chopper of the first type in Fig. 18 was operated. (a) time spectra at 150° counter, (b) a part of (a) indicated by a horizontal line is plotted in an enlarged scale. (c) time spectra of 24th 1D-PSD, where positional information was disregarded. (d)time spectra of direct beam obtained with 22th 1D-PSD which corresponds to the case of elastic scattering.

Fig. 20 (a) Small angle scattering from Fe_3Pt, plotted against Q for different wavelengths, (b) that plotted against scattering angle .

Fig. 21 Time variation of small angle scattering from $90FeTiO_3$-$10Fe_2O_3$, when a squared pulsed magnetic field of 5 kOe was applied to the sample.

Fig. 22 Block diagram of data acquisition system for real time spectroscopy.

Fig. 23 Energy spectrum of solid methane cold moderator at 20K, compared with that of polyethylene plate at 295 K.

Fig. 24 Beam divergence of neutrons with and without guide and with an appropriate collimator.

Fig. 25 Wavelength dependence of neutron intensity at different positions. SG(9m) (SG(19 m)): at the exit of straight neutron guide 9m (19 m), far from cold neutron source, BG: at the exist of bent guide with a cut off wavelength λ_c = 4 A. NG: at the position of 19 m far from cold moderator, but without guide.

KENS-SAN Arrangement

(a)

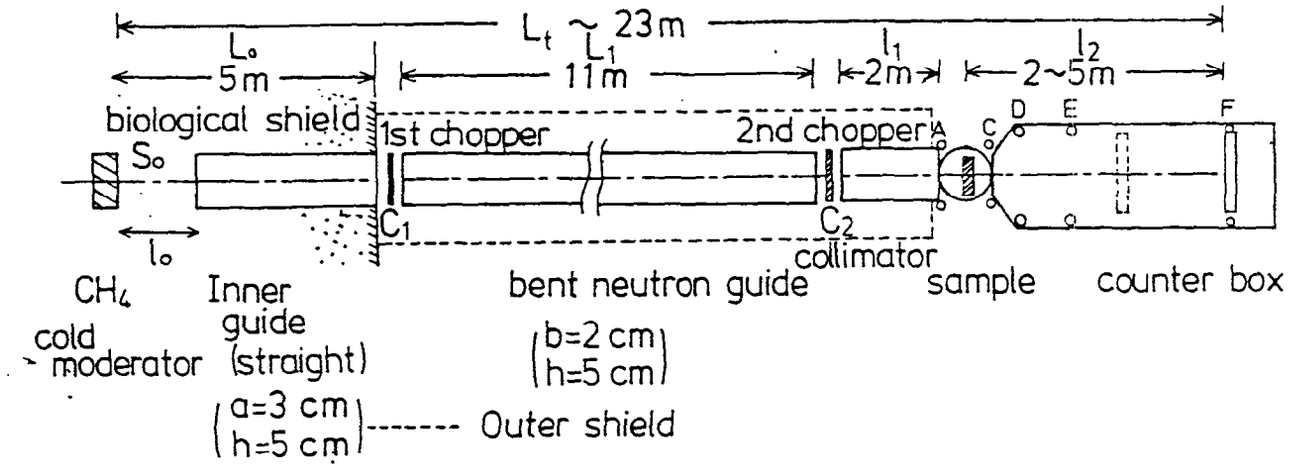

(b)

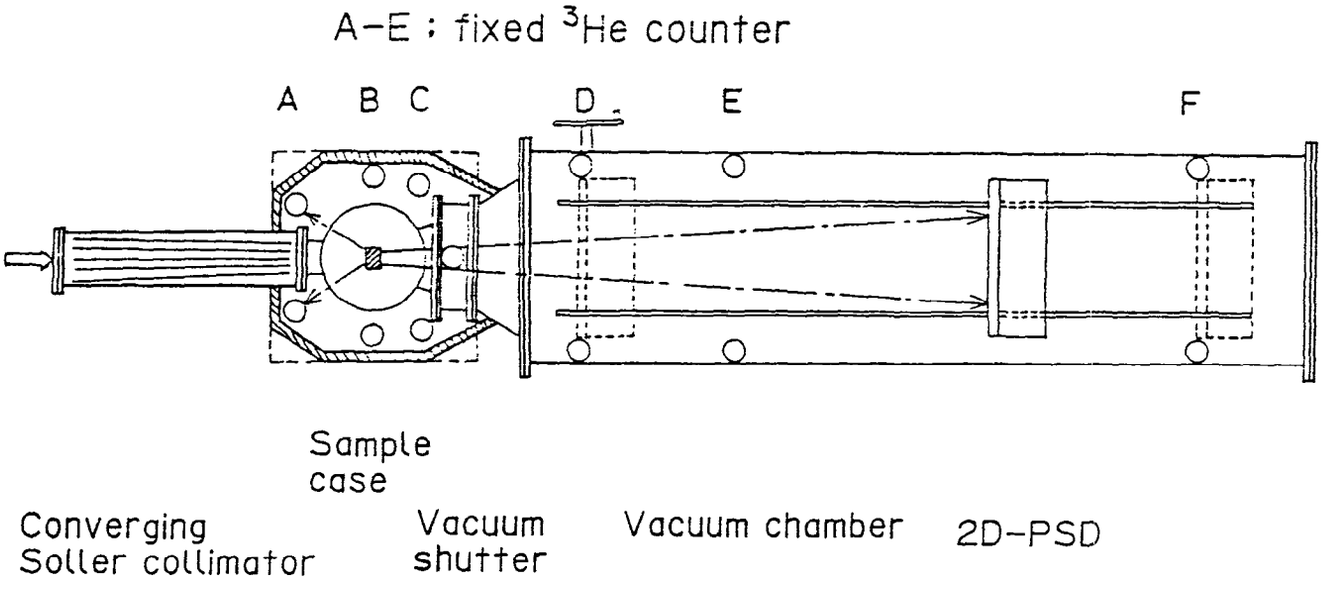

Fig. 1

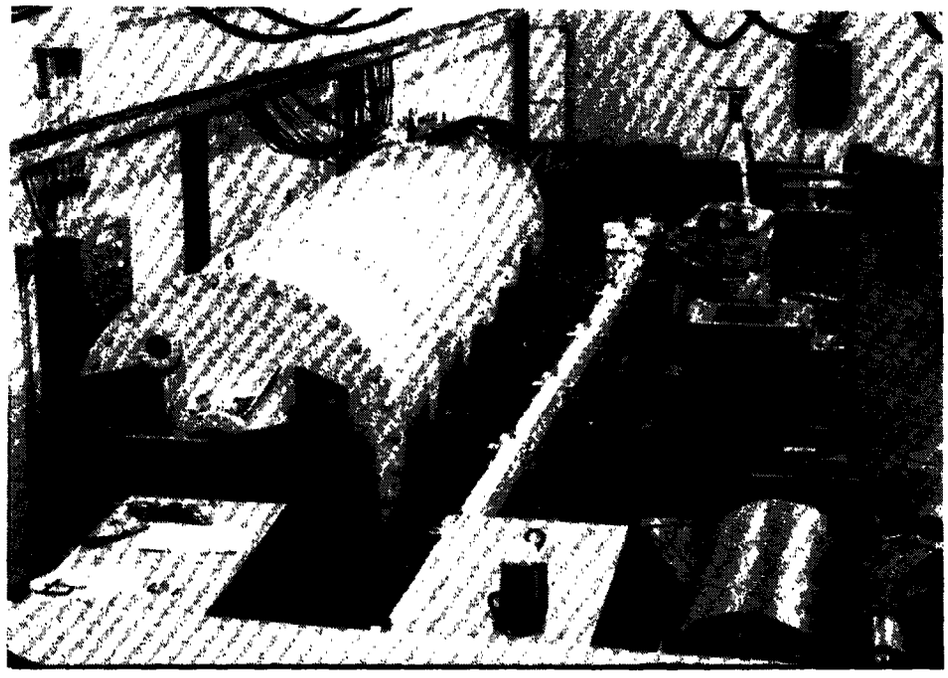

(a)

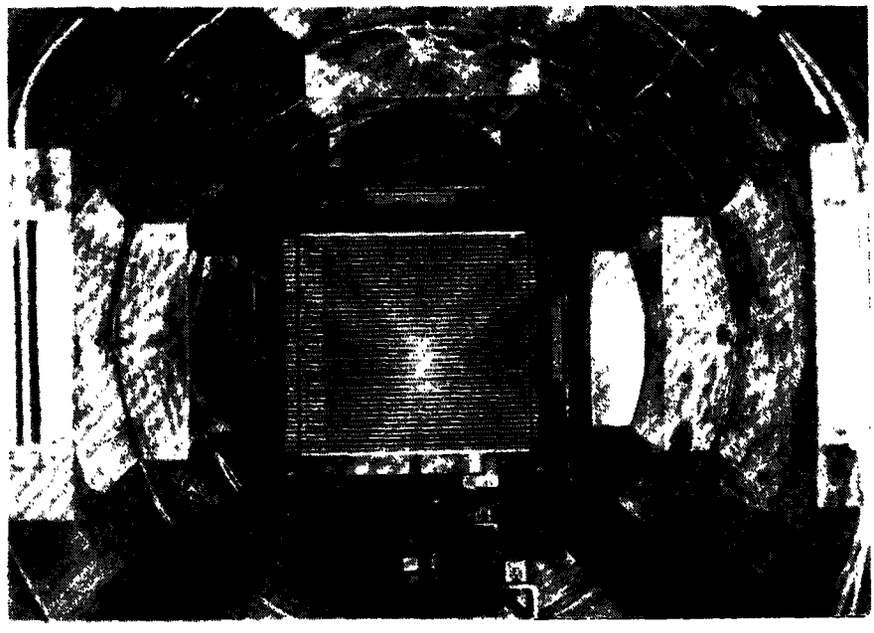

(b)

Fig. 2

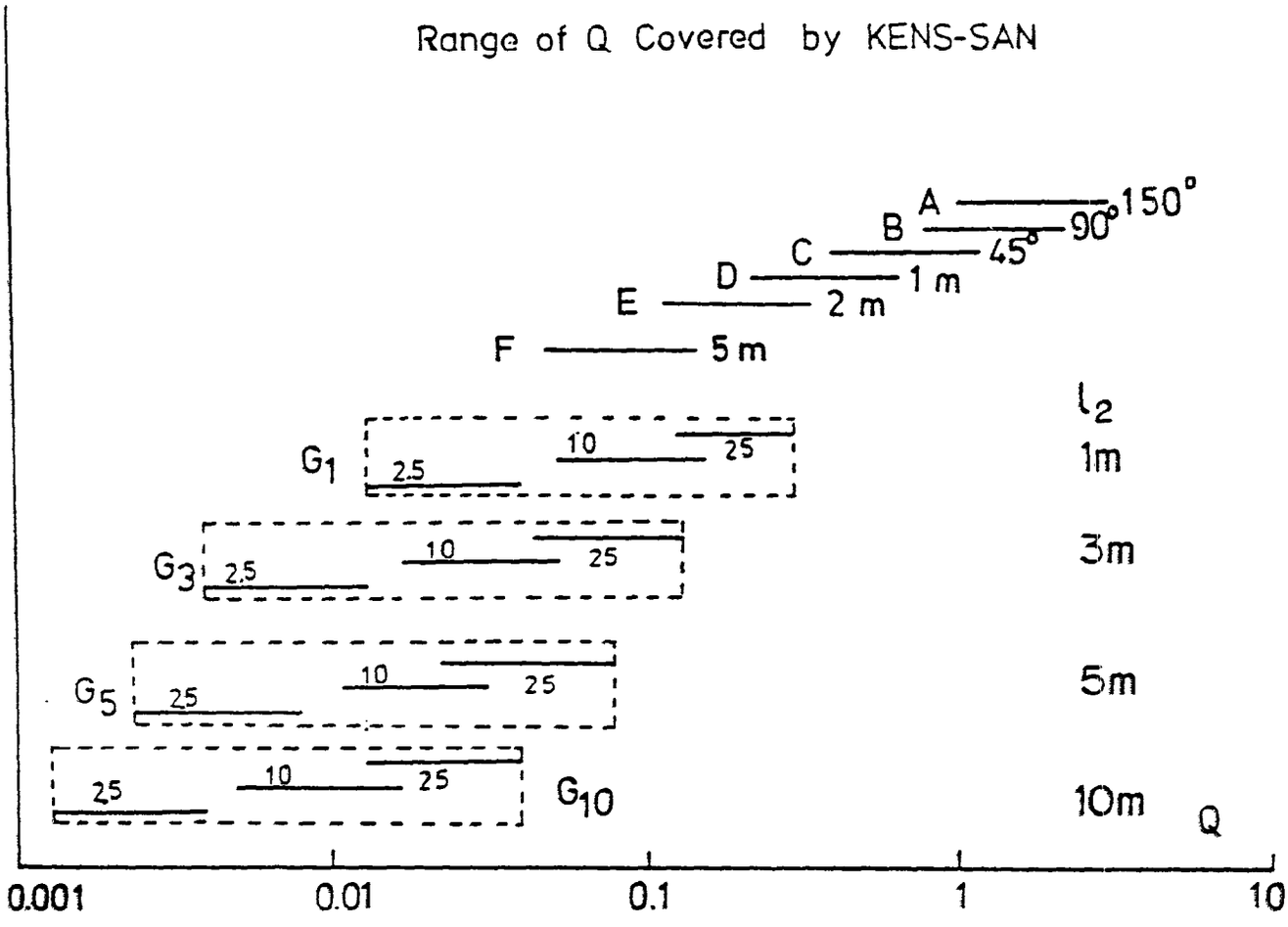
Range of Q Covered by KENS-SAN
A
150°
B
90°
C
45°
D
1 m
E
2 m
F
5 m
l_2
G_1
2.5
10
25
1m
G_3
2.5
10
25
3m
G_5
2.5
10
25
5m
2.5
10
25
G_{10}
10m
Q
0.001
0.01
0.1
1
10

Fig. 3

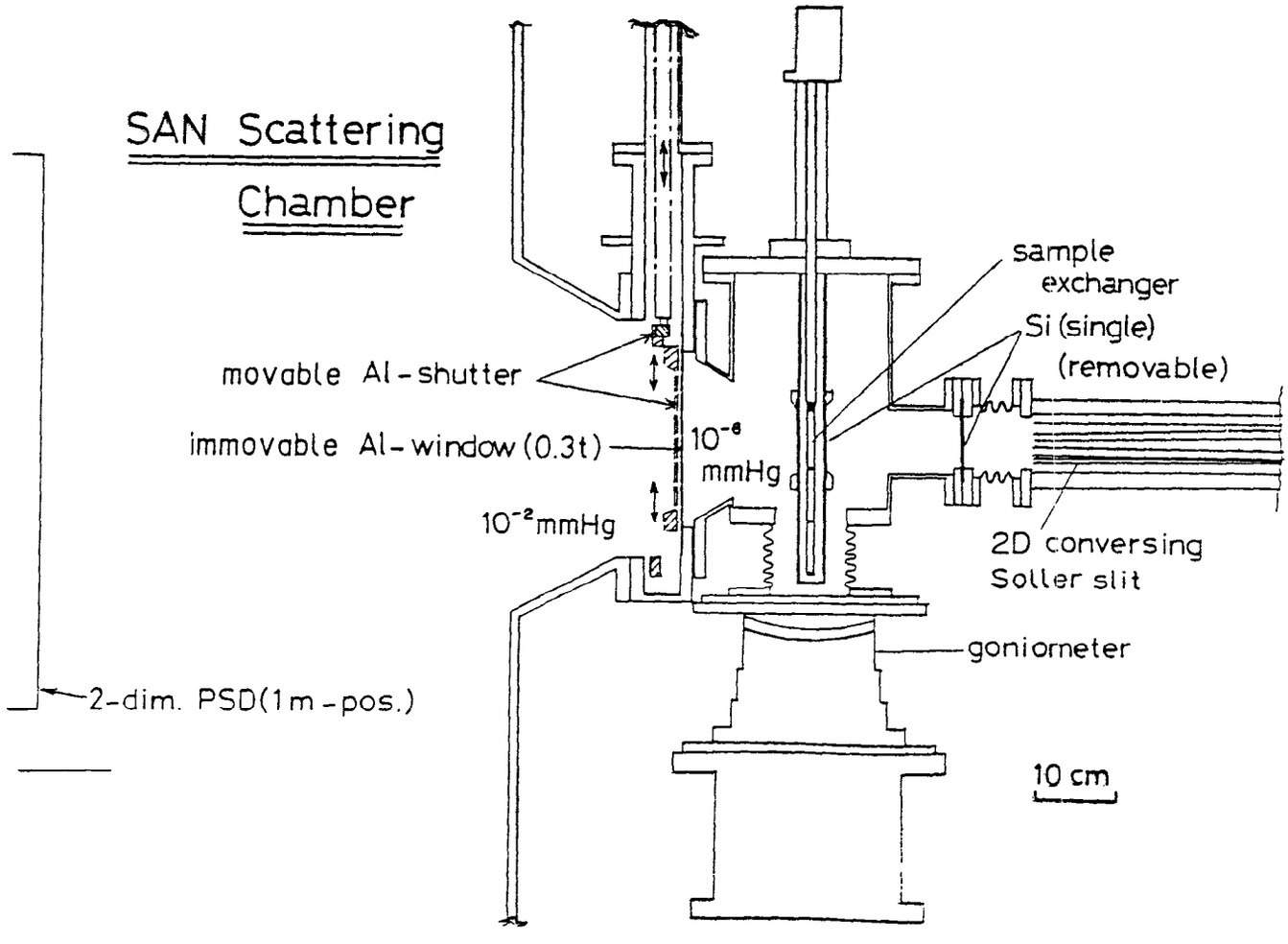
SAN Scattering
Chamber
sample
exchanger
Si (single)
(removable)
movable Al-shutter
immovable Al-window (0.3t)
10^{-6}
mmHg
10^{-2}mmHg
2D conversing
Soller slit
goniometer
2-dim. PSD(1m-pos.)
10 cm

Fig. 4

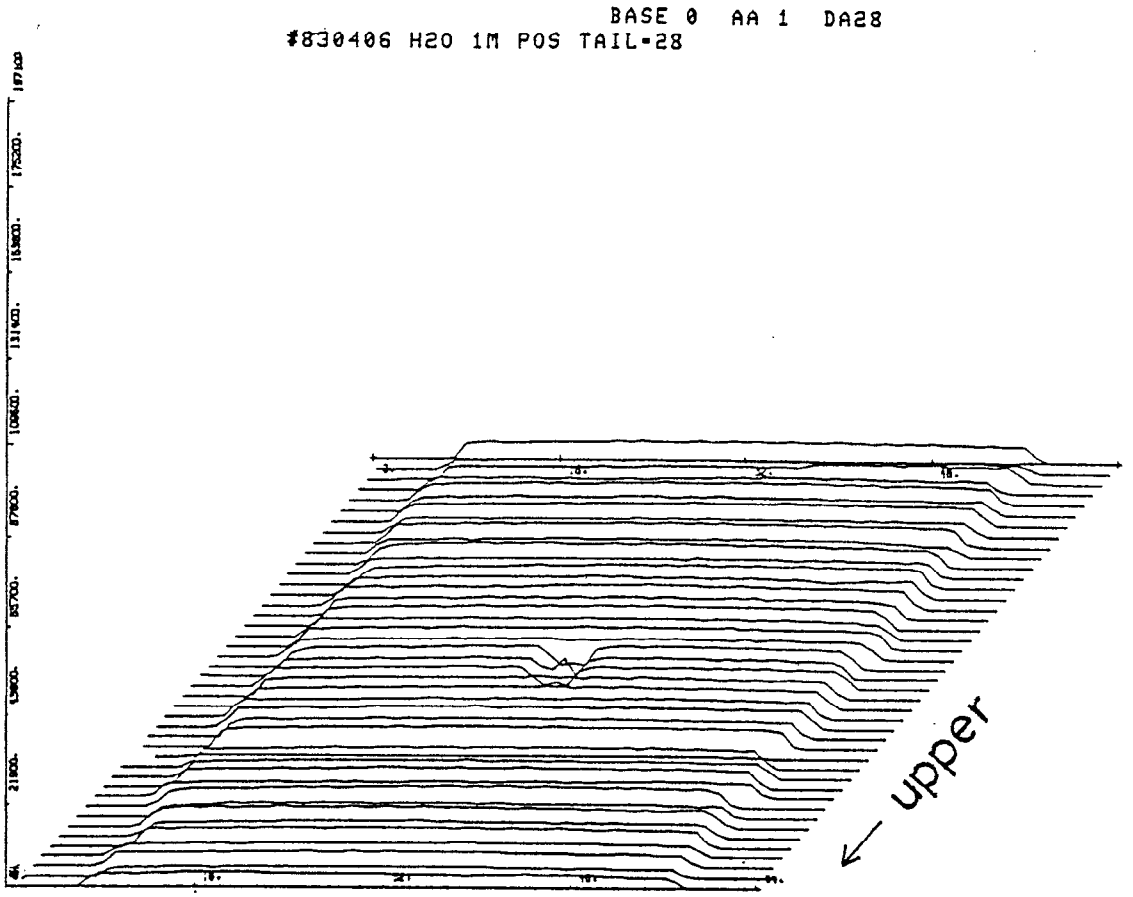

(b)

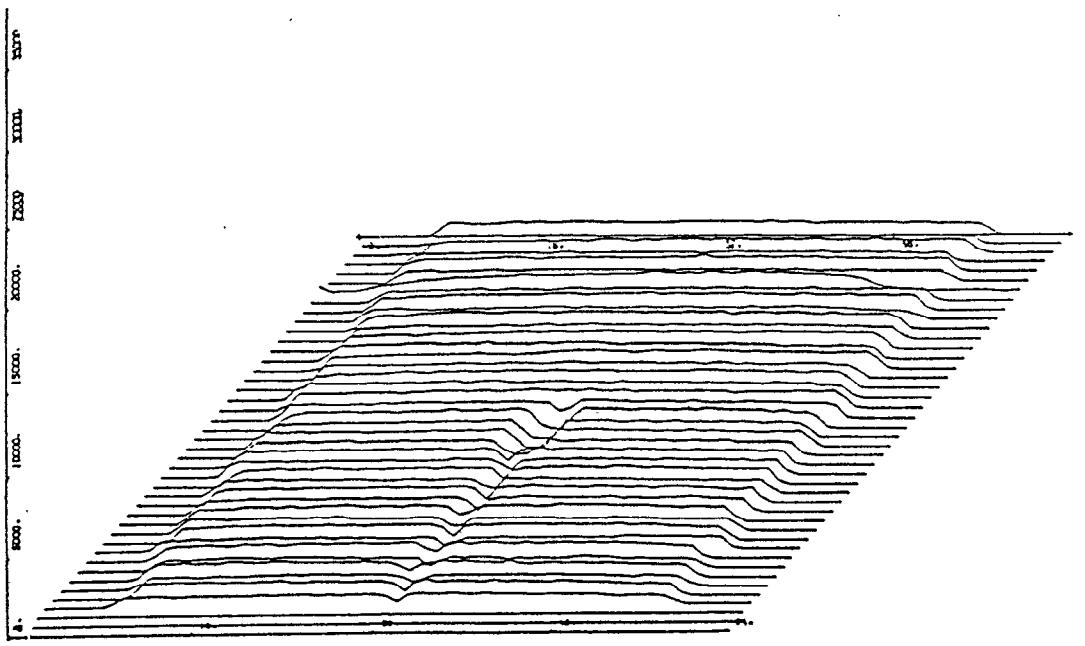

(a)

Fig. 5

(a) SAN 2-dim. PSD & Beam Stopper

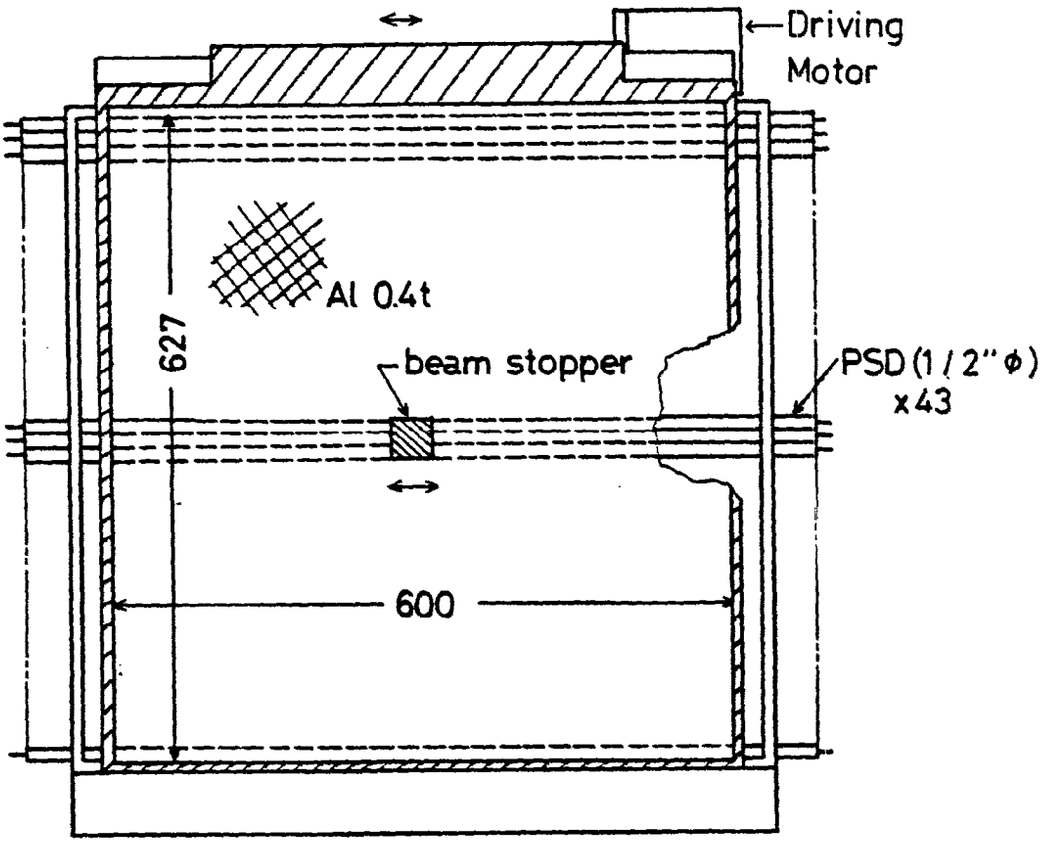

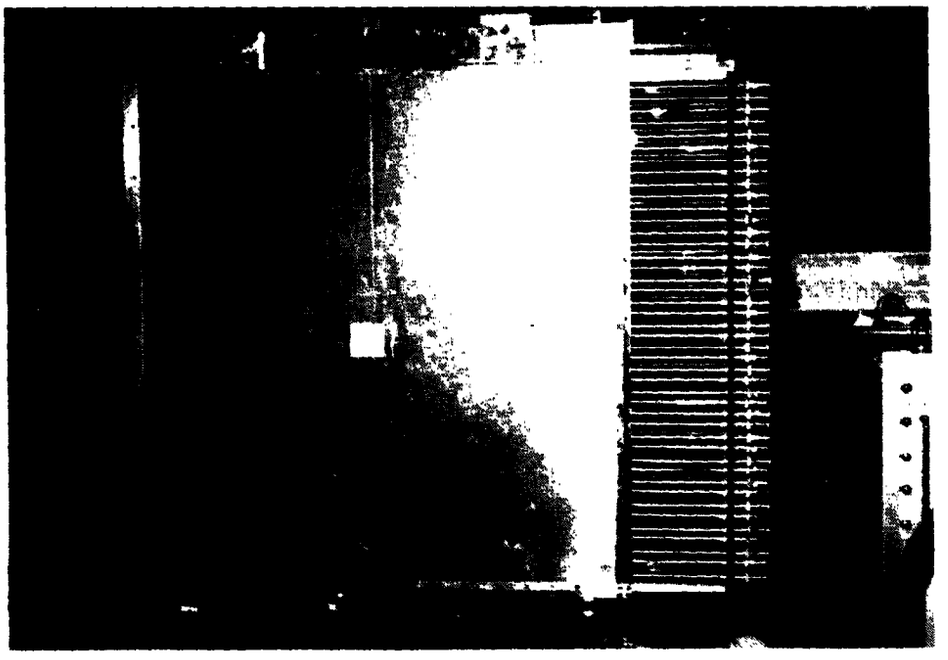

Fig. 6

(a) Converging Slit Collimator System.

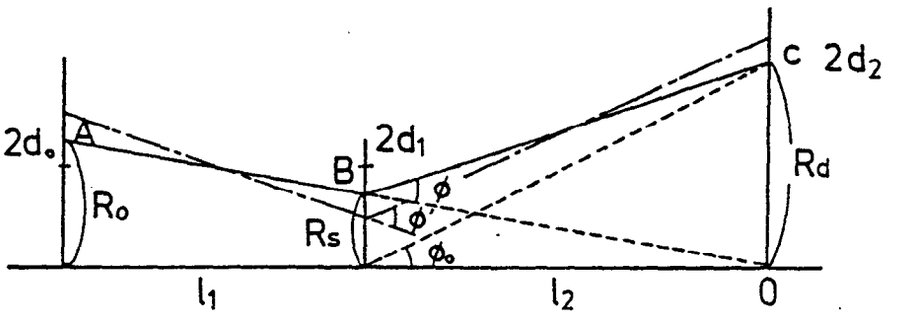

(b) Non Converging Condition

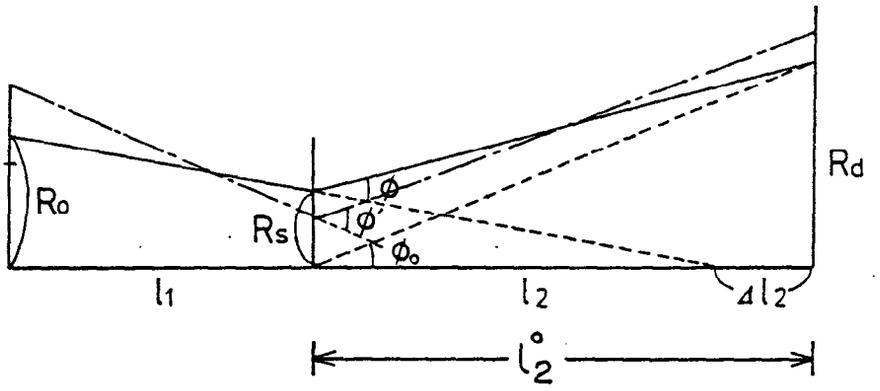

Fig. 7

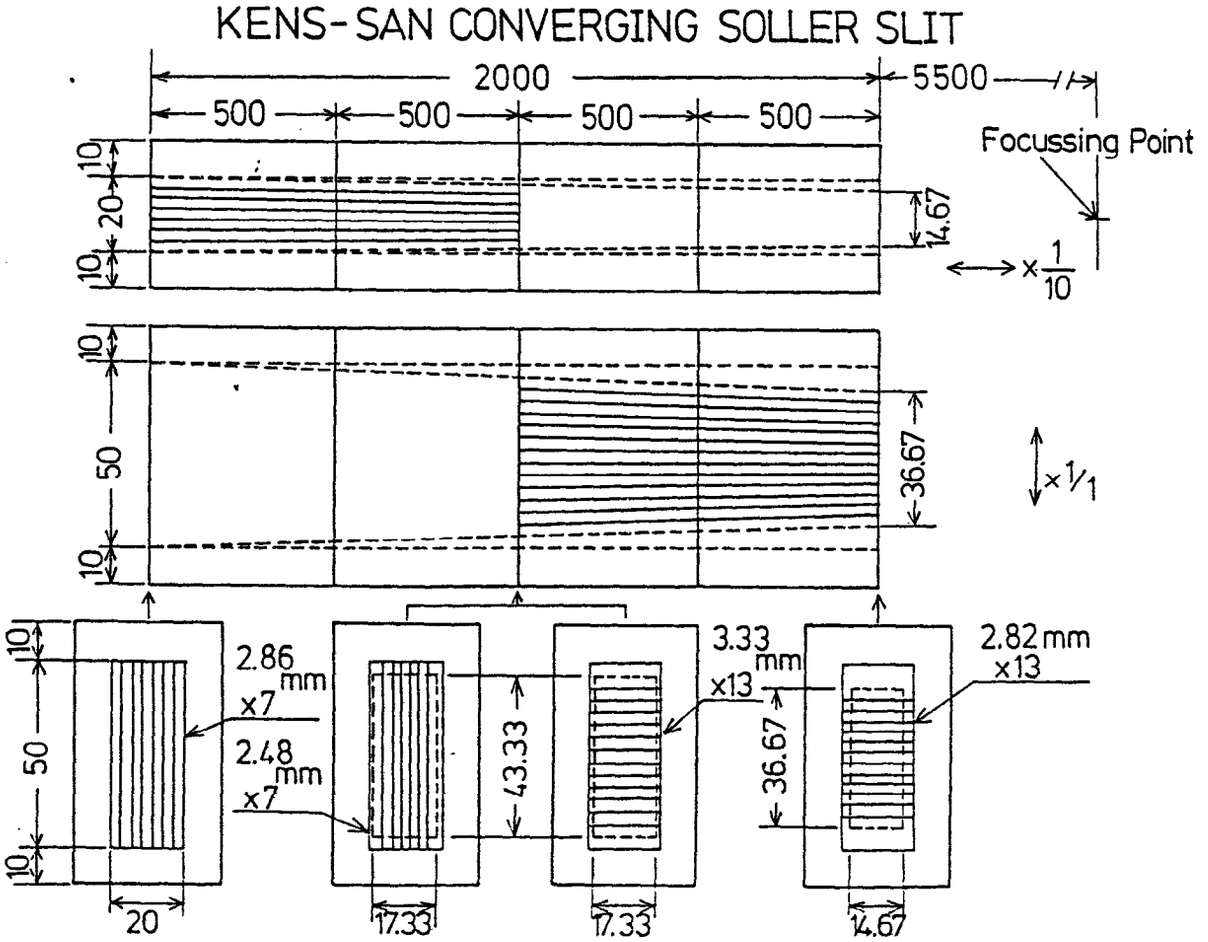

Fig. 8

Direct Beam Profiles

(5m position)

with collimator

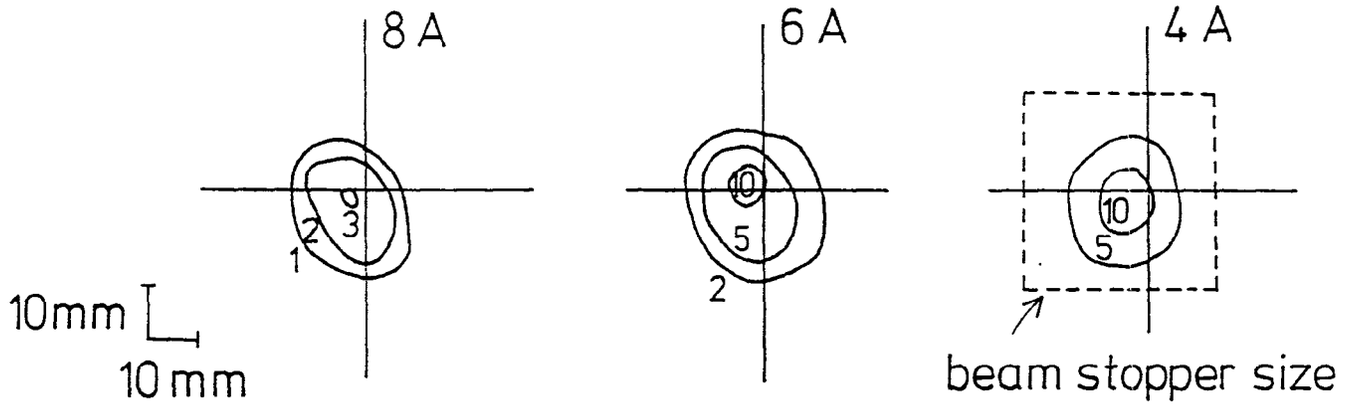

without collimator.

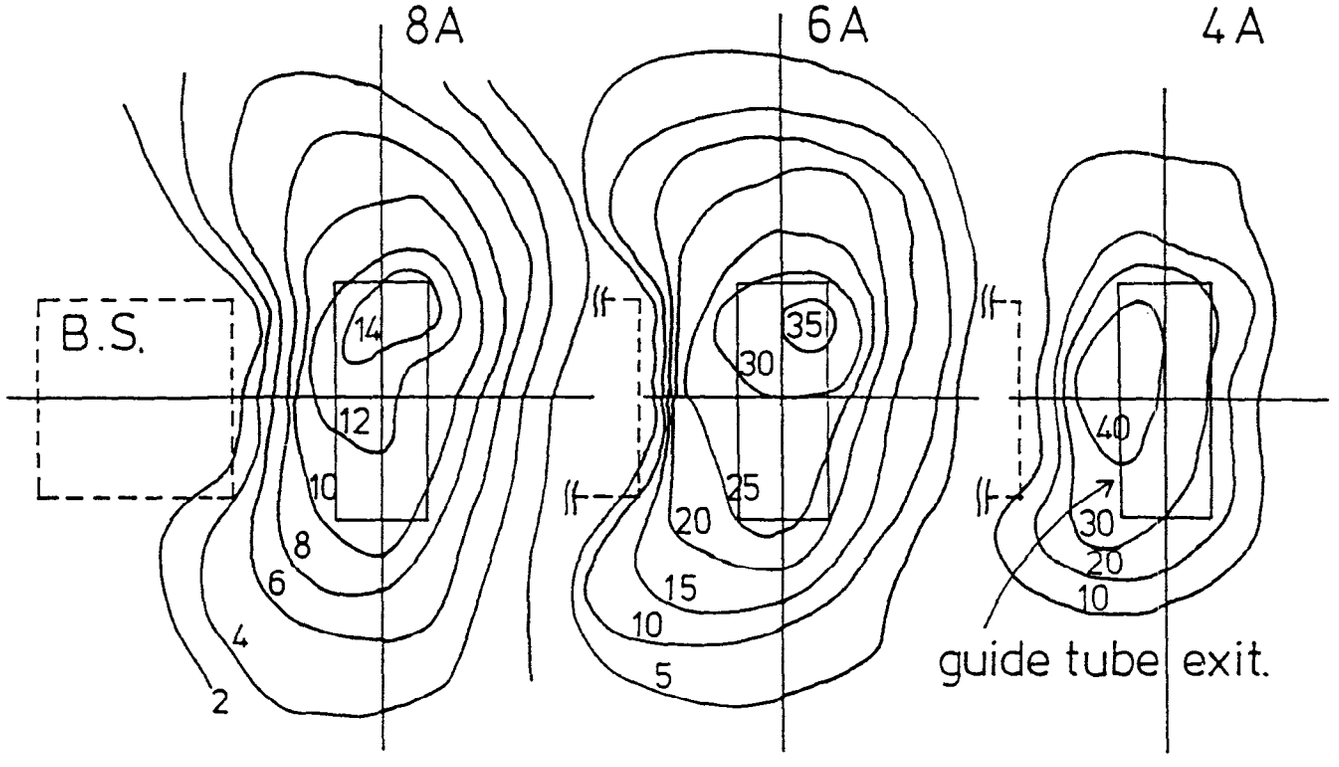

Fig. 9

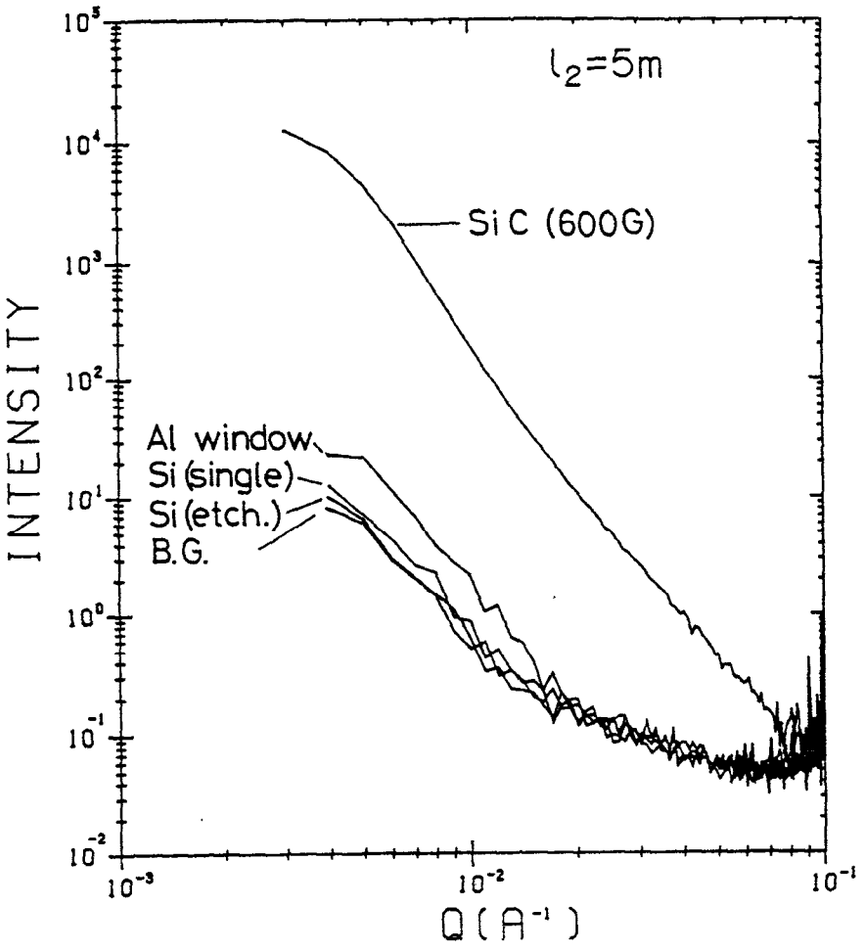
l_2=5m
Si C (600G)
Al window
Si (single)
Si (etch.)
B.G.
INTENSITY
Q (A^{-1})

Fig. 10

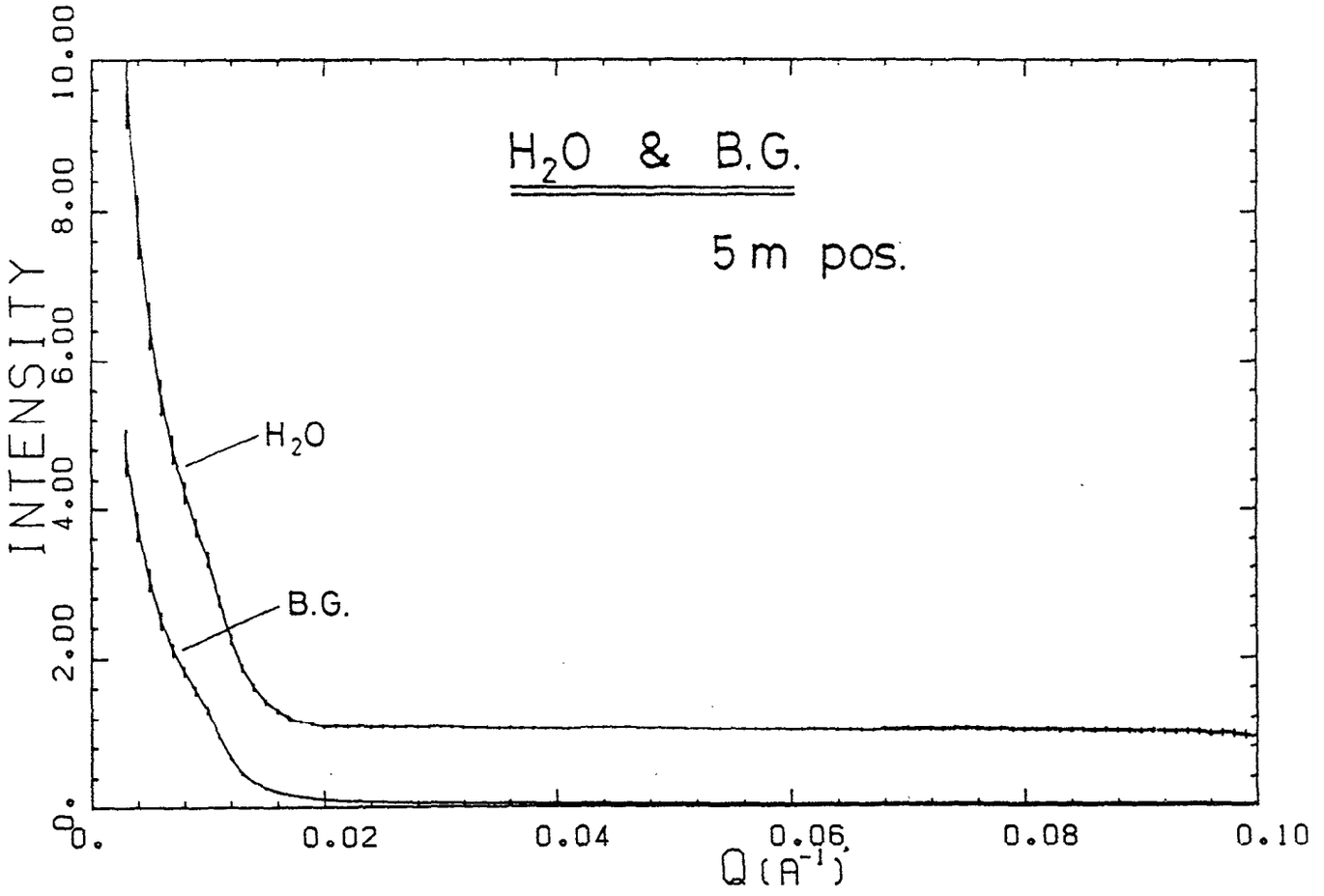
H_2O & B.G.
5 m pos.
H_2O
B.G.
INTENSITY
Q (A^{-1})

Fig. 11

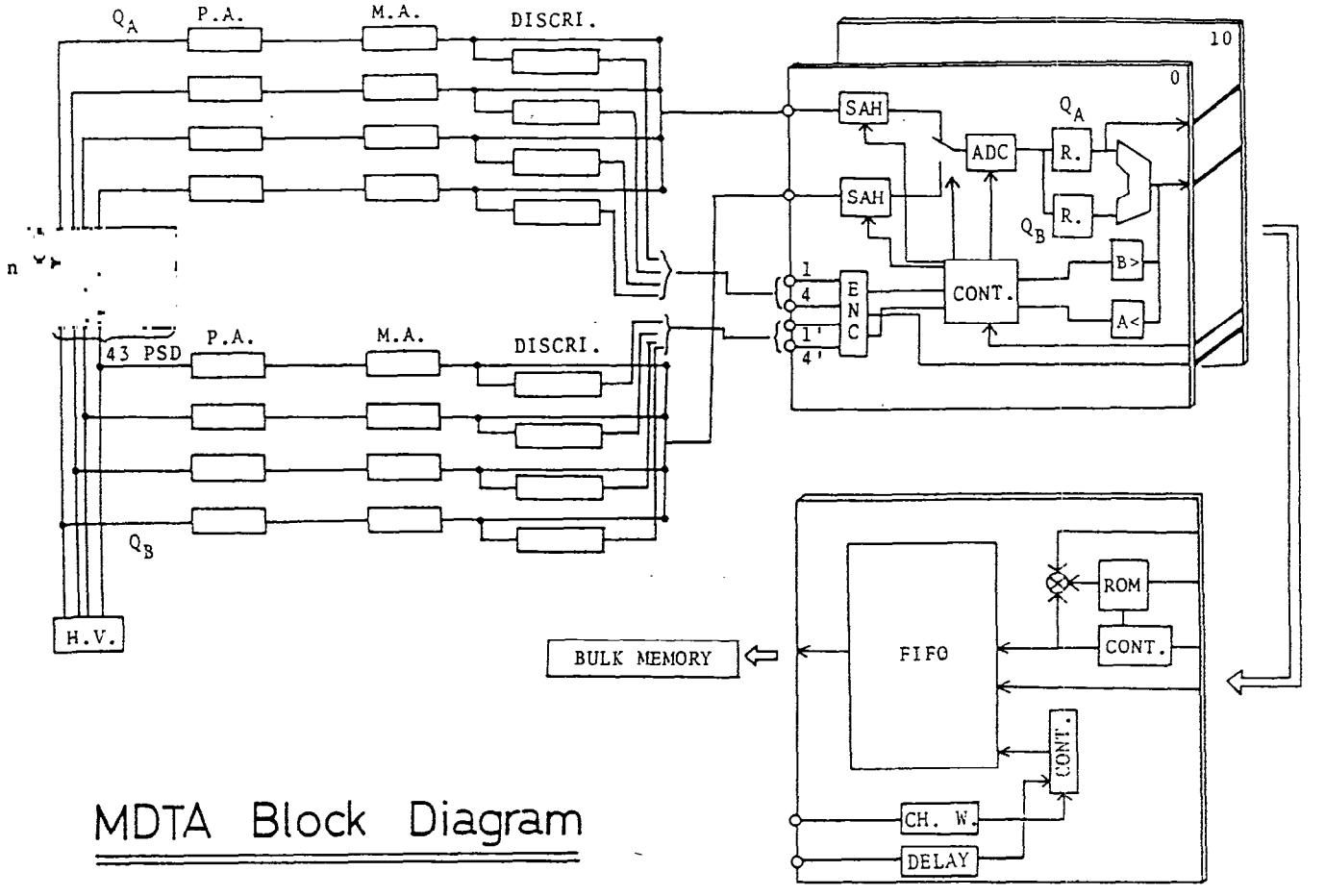
Q_A
P.A.
M.A.
DISCRI.
10
0
SAH
SAH
ADC
Q_A
R.
R.
Q_B
B>
A<
CONT.
1
4
1'
4'
E
N
C
43 PSD
P.A.
M.A.
DISCRI.
Q_B
H.V.
BULK MEMORY
FIFO
ROM
CONT.
CONT.
CH. W.
DELAY
MDTA Block Diagram

Fig. 12

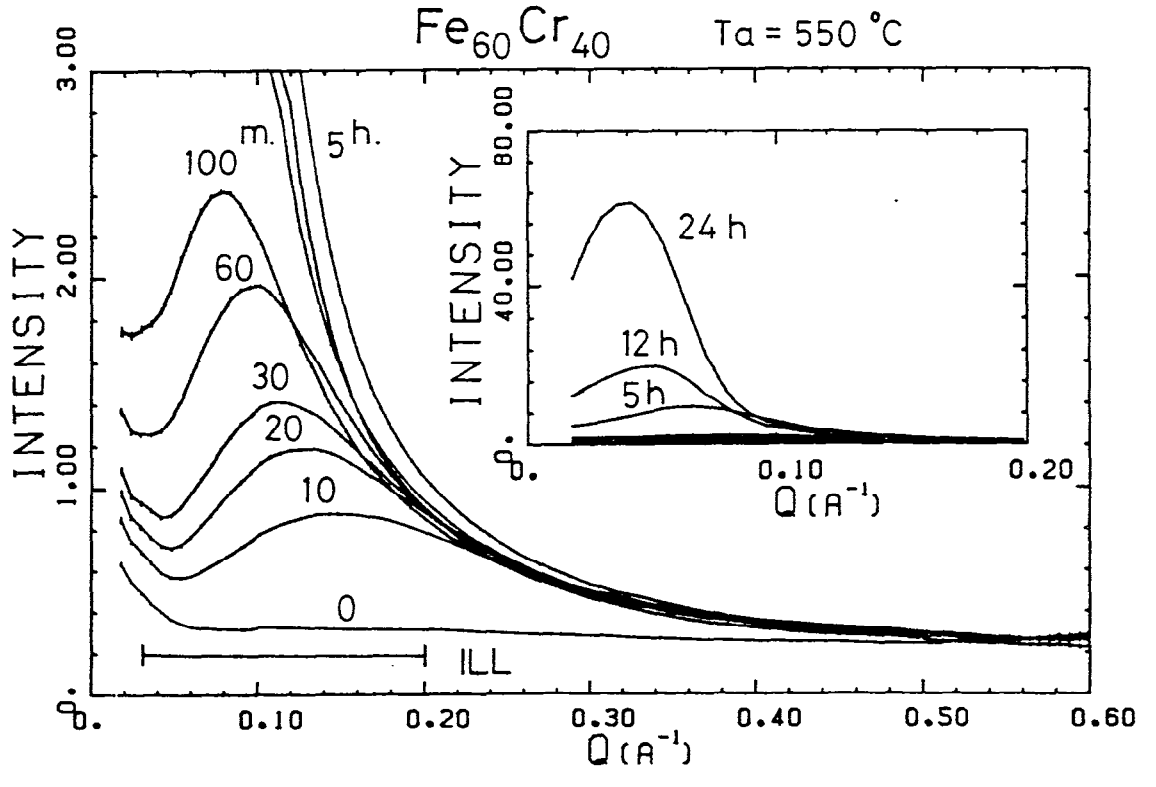
$Fe_{60}Cr_{40}$
Ta = 550 °C
INTENSITY
3.00
2.00
1.00
0.
100
m.
5 h.
60
30
20
10
0
ILL
0.10
0.20
0.30
0.40
0.50
0.60
Q(A^{-1})
INTENSITY
80.00
40.00
0.
24 h
12 h
5h
0.10
0.20
Q(A^{-1})

Fig. 13

$90FeTiO_3-10Fe_2O_3$

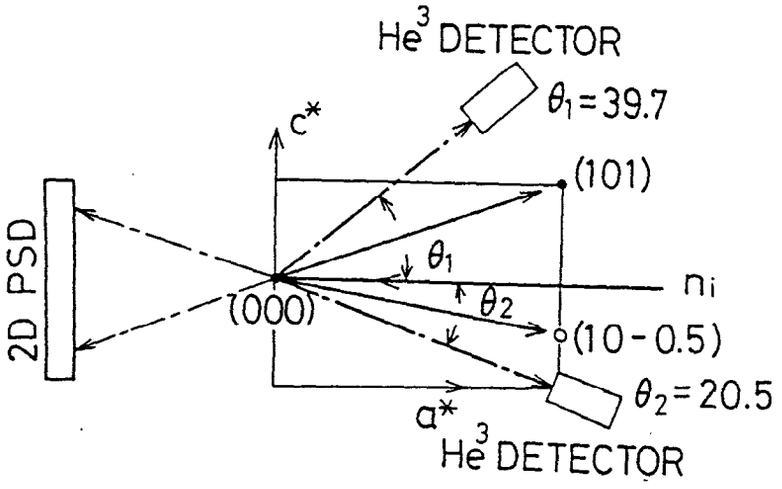

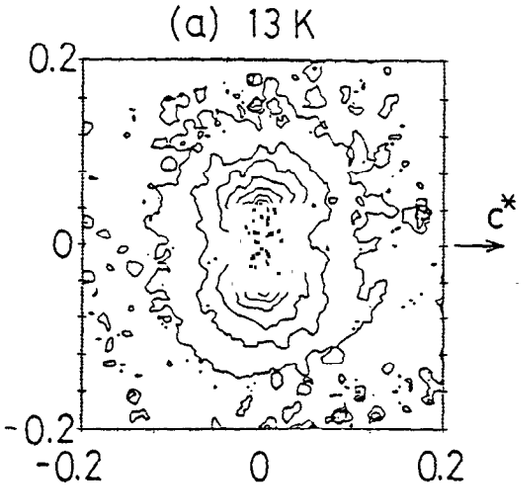

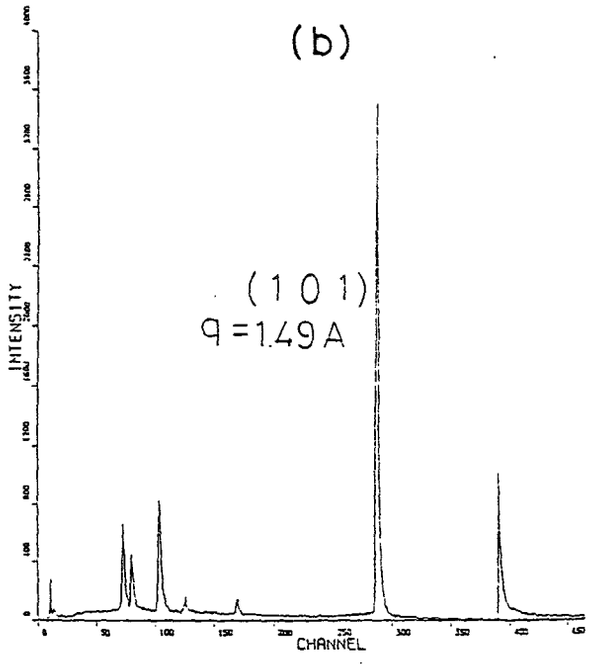

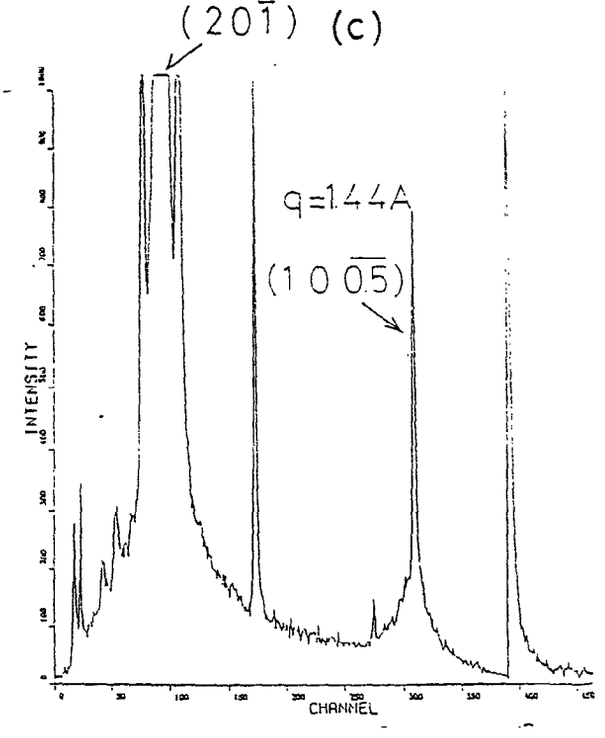

Fig. 14

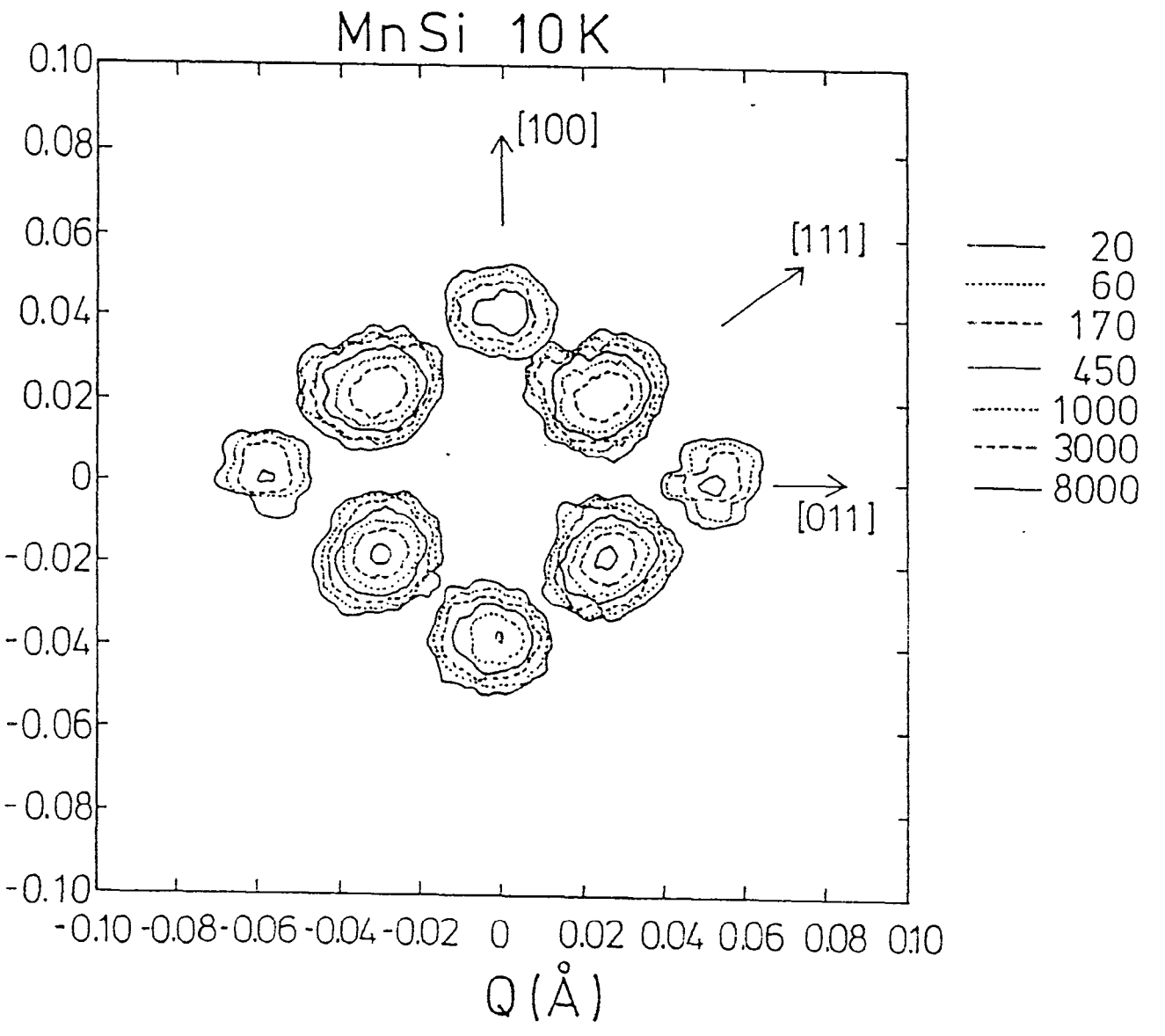
MnSi 10K
[100]
[111]
[011]
20
60
170
450
1000
3000
8000
0.10
0.08
0.06
0.04
0.02
0
-0.02
-0.04
-0.06
-0.08
-0.10
-0.10 -0.08 -0.06 -0.04 -0.02 0 0.02 0.04 0.06 0.08 0.10
Q(Å)

Fig. 15

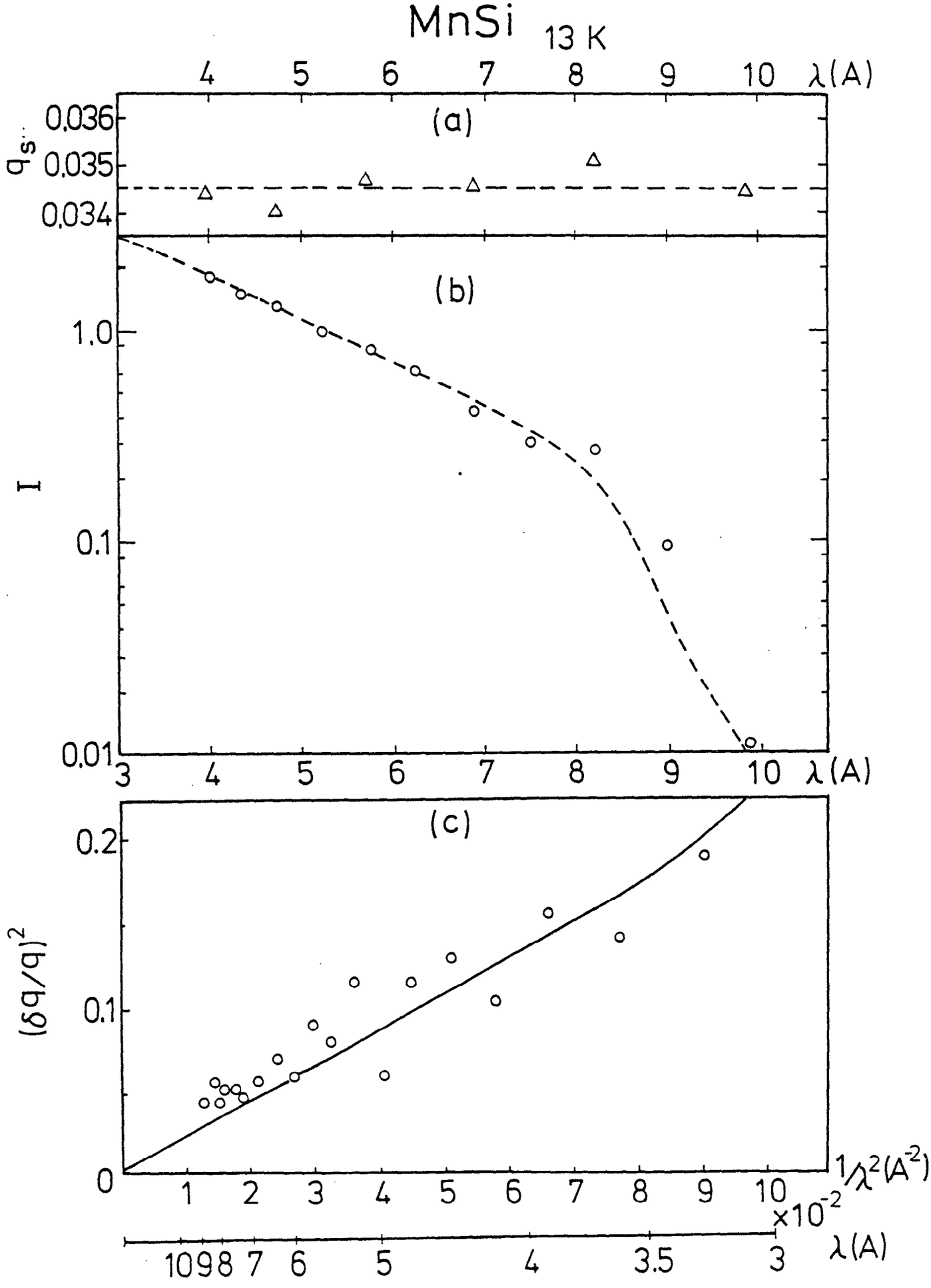
MnSi 13 K
4 5 6 7 8 9 10 λ(A)
(a)
q_s
0,036
0,035
0,034
(b)
I
1.0
0.1
0.01
3 4 5 6 7 8 9 10 λ(A)
(c)
$(\delta q/q)^2$
0.2
0.1
0
1 2 3 4 5 6 7 8 9 10
$1/\lambda^2(A^{-2})$
$\times 10^{-2}$
10 9 8 7 6 5 4 3.5 3
λ(A)

Fig. 16

(a)

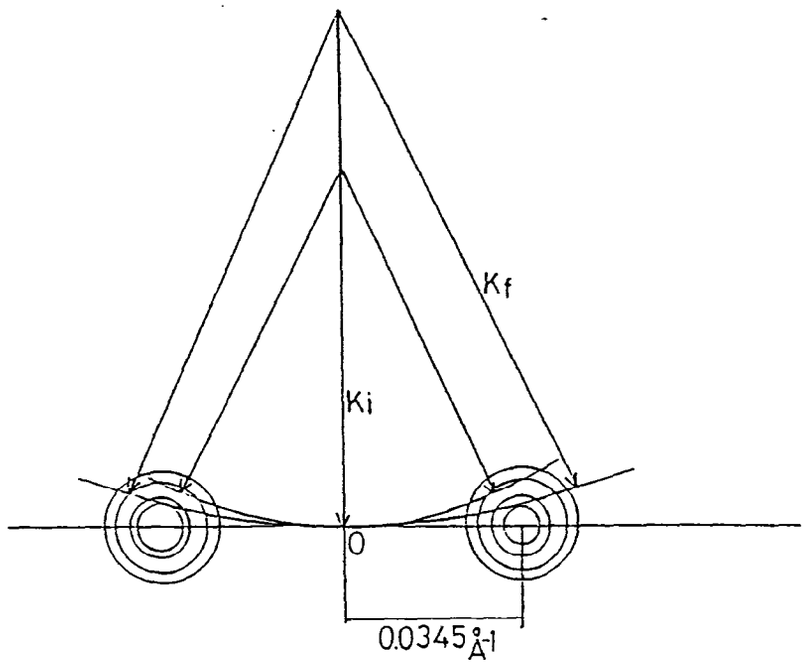
Kf
Ki
0
0.0345Å-1

(b)

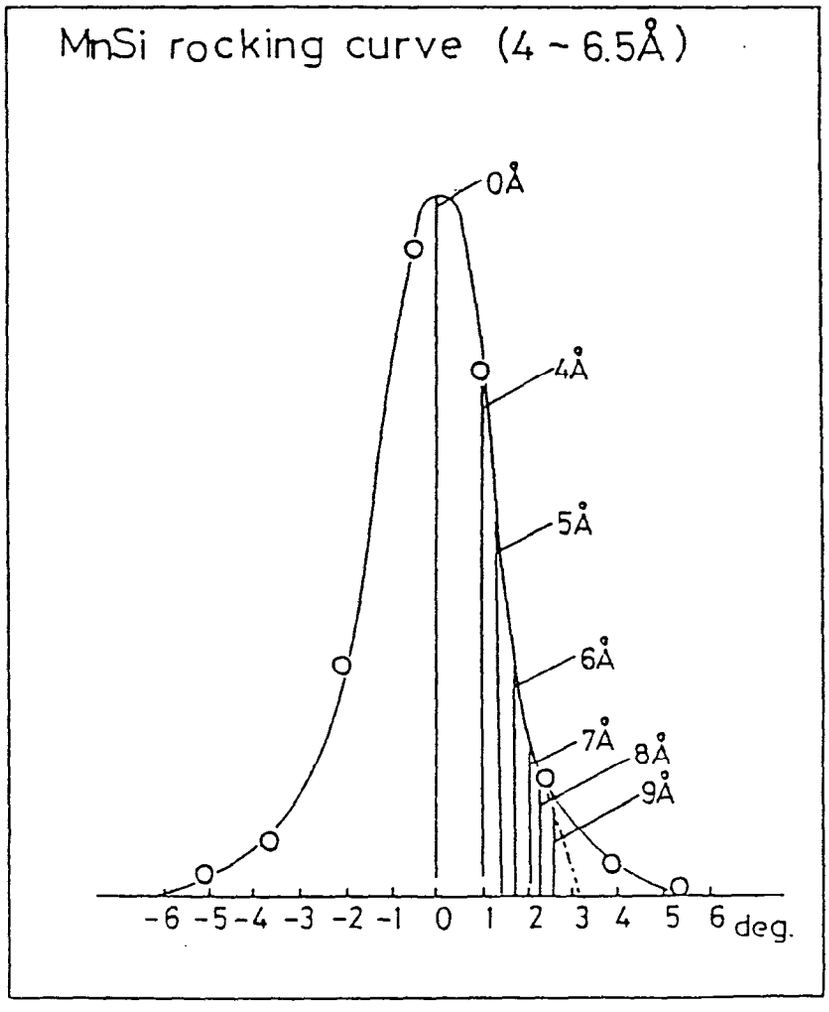
MnSi rocking curve (4 ~ 6.5Å)
0Å
4Å
5Å
6Å
7Å
8Å
9Å
-6 -5 -4 -3 -2 -1 0 1 2 3 4 5 6 deg.

Fig. 17

(1) Chopper for Rejecting Inelastic Part

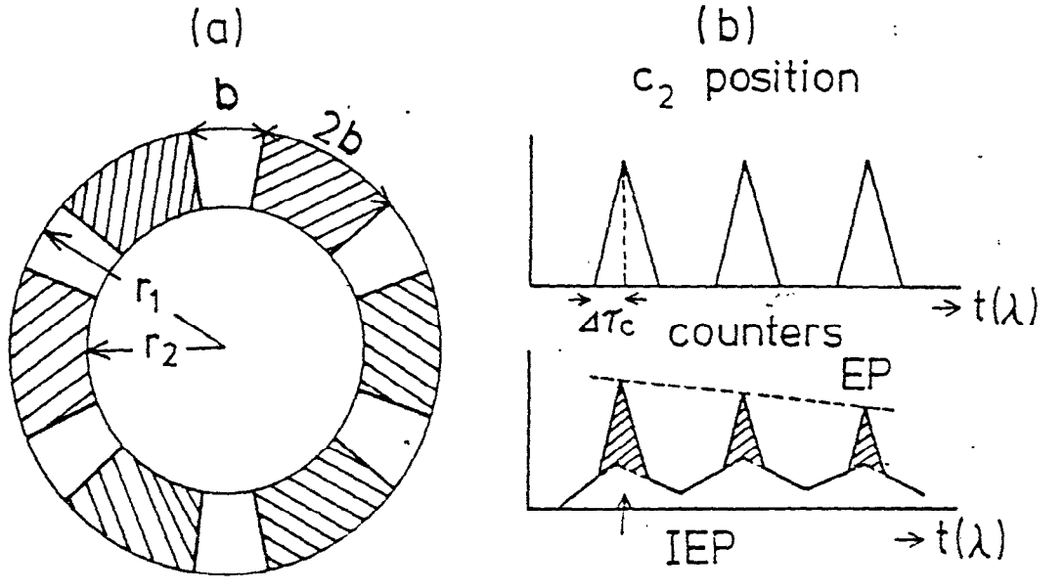

(2) Chopper for Inelastic Scattering

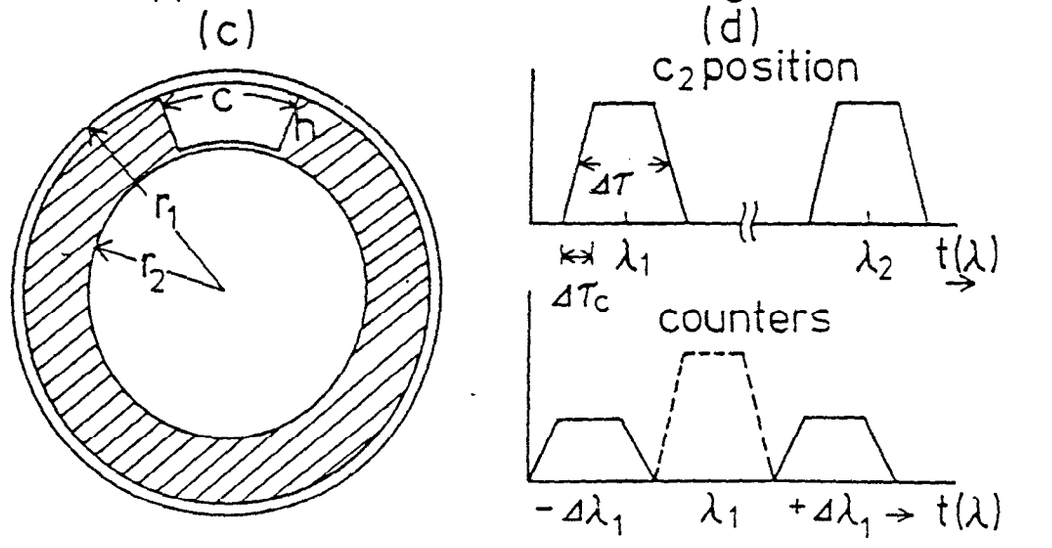

Fig. 18

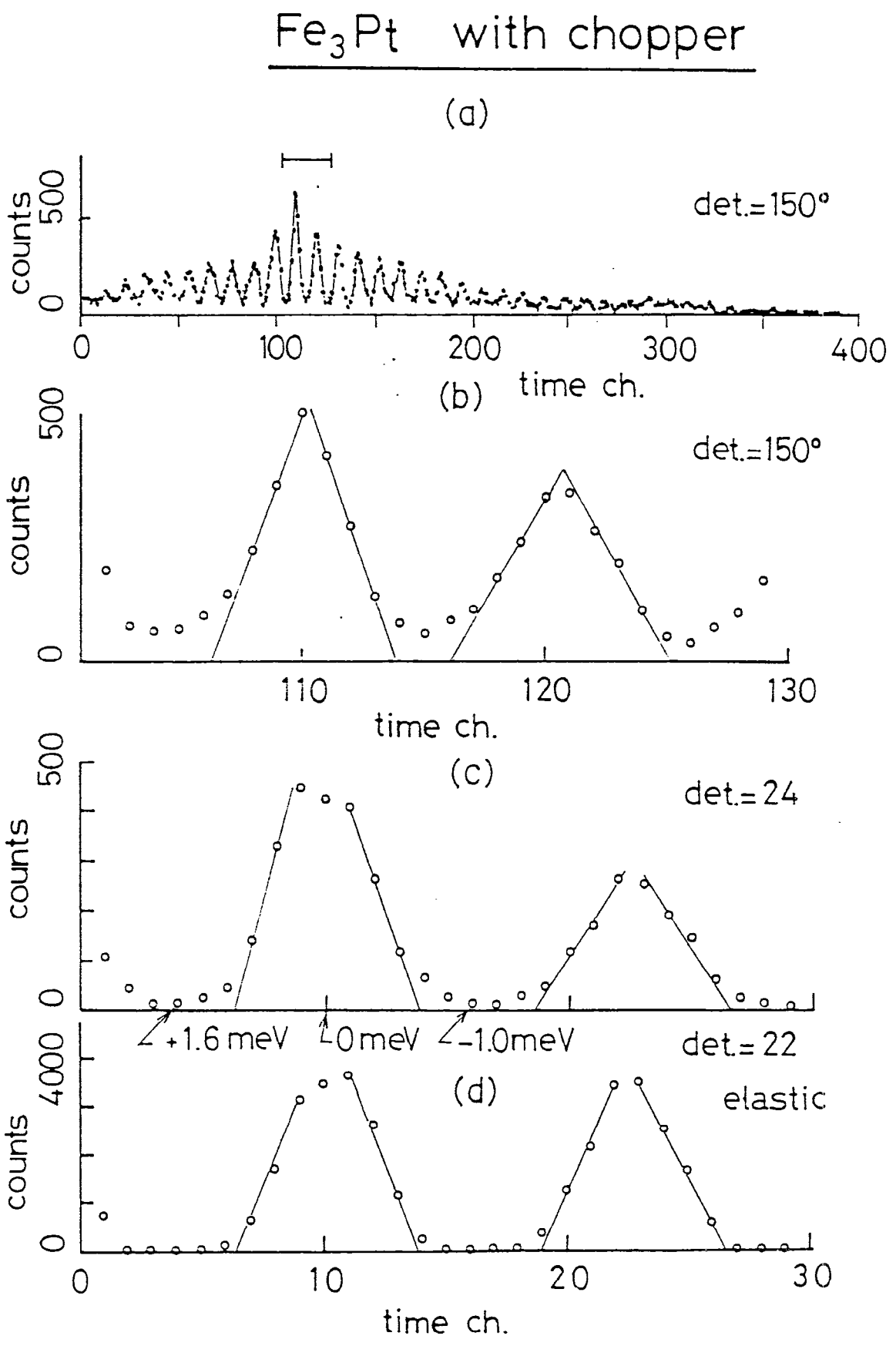
Fe3Pt with chopper
(a)
counts
500
0
det.=150°
0
100
200
300
400
time ch.
(b)
counts
500
0
det.=150°
110
120
130
time ch.
(c)
counts
500
0
det.= 24
+1.6 meV
0 meV
-1.0meV
(d)
counts
4000
0
det.= 22
elastic
0
10
20
30
time ch.

Fig. 19

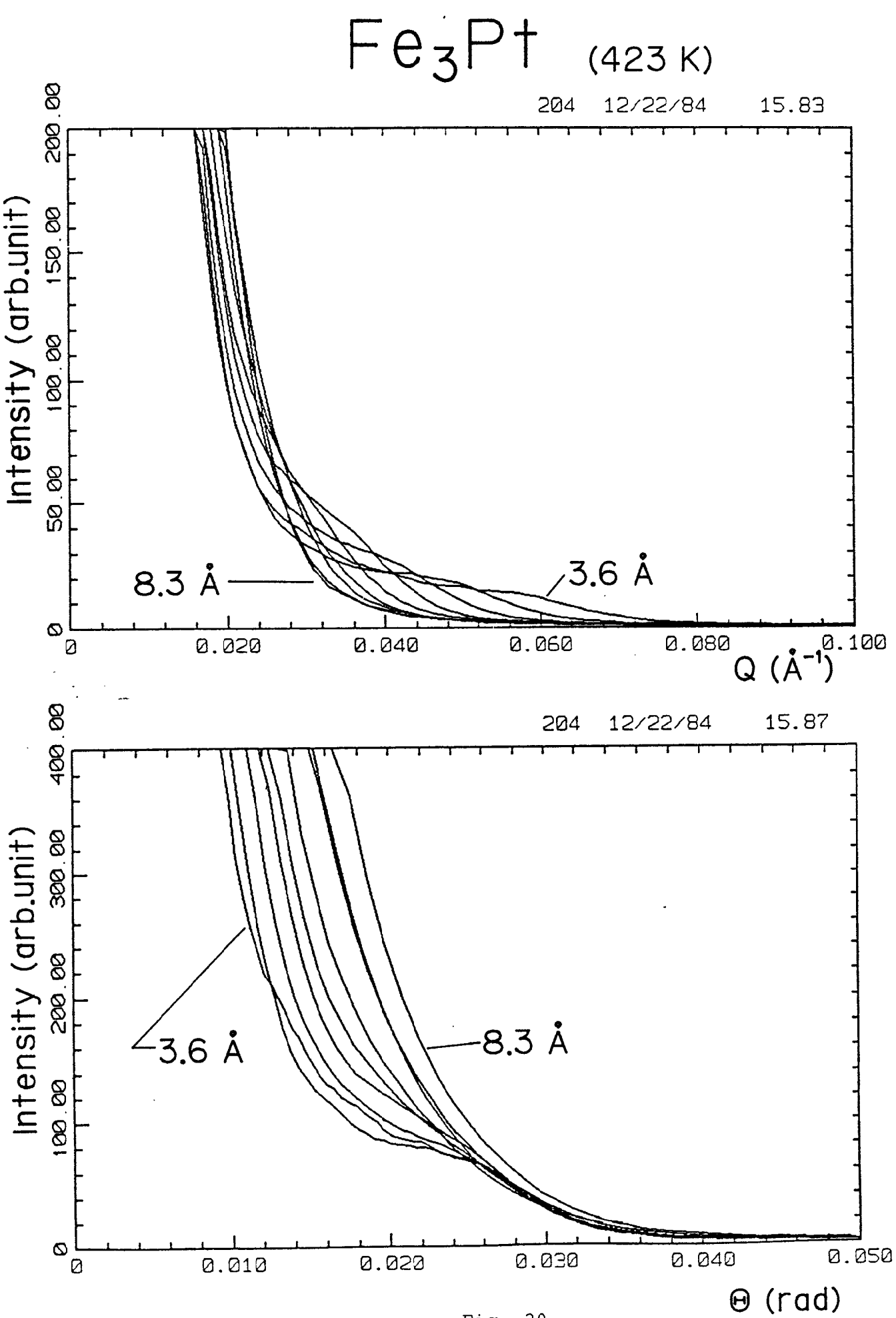
Fe3Pt (423 K)
204 12/22/84 15.83
Intensity (arb.unit)
200.00
150.00
100.00
50.00
0
8.3 Å
3.6 Å
0
0.020
0.040
0.060
0.080
0.100
Q (Å-1)
204 12/22/84 15.87
Intensity (arb.unit)
400.00
300.00
200.00
100.00
0
3.6 Å
8.3 Å
0
0.010
0.020
0.030
0.040
0.050
Θ (rad)

Fig. 20

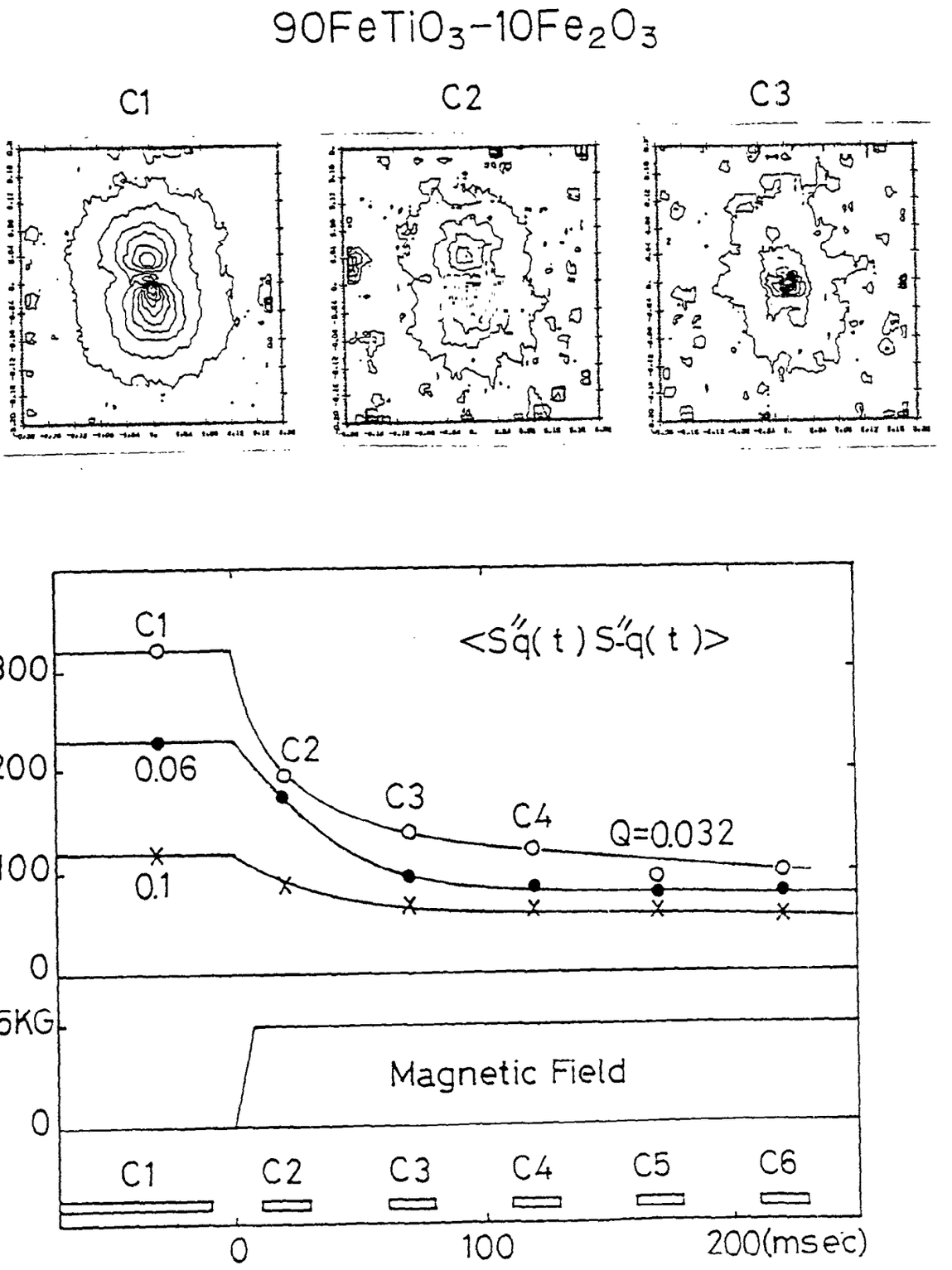
90FeTiO3-10Fe2O3
C1
C2
C3
<S''q(t) S-''q(t)>
Intensity
300
200
100
0
0.06
0.1
C1
C2
C3
C4
Q=0.032
5KG
0
Magnetic Field
C1
C2
C3
C4
C5
C6
0
100
200(msec)

Fig. 21

BLOCK DIAGRAM OF THE BULK MEMORY

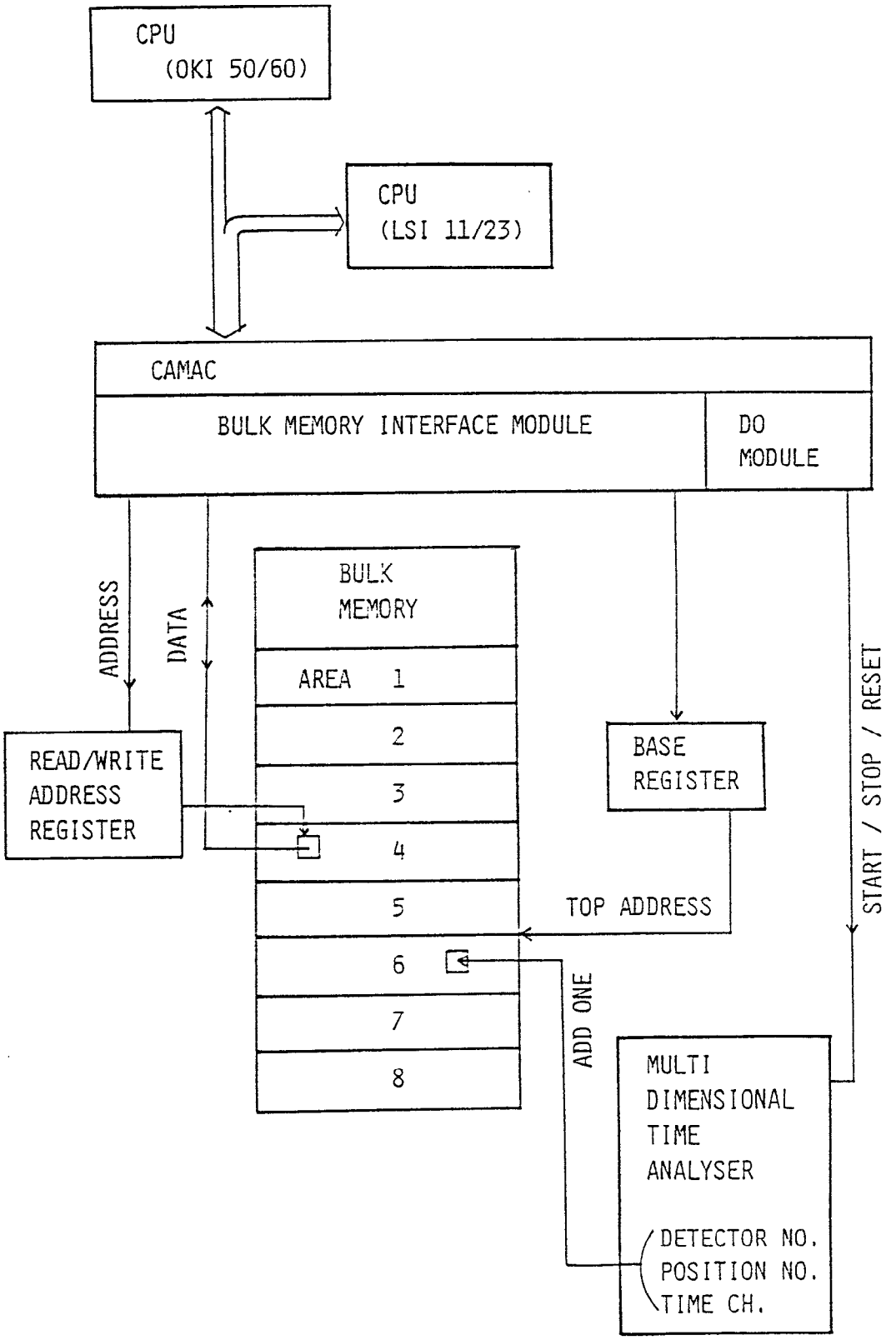

Fig. 22

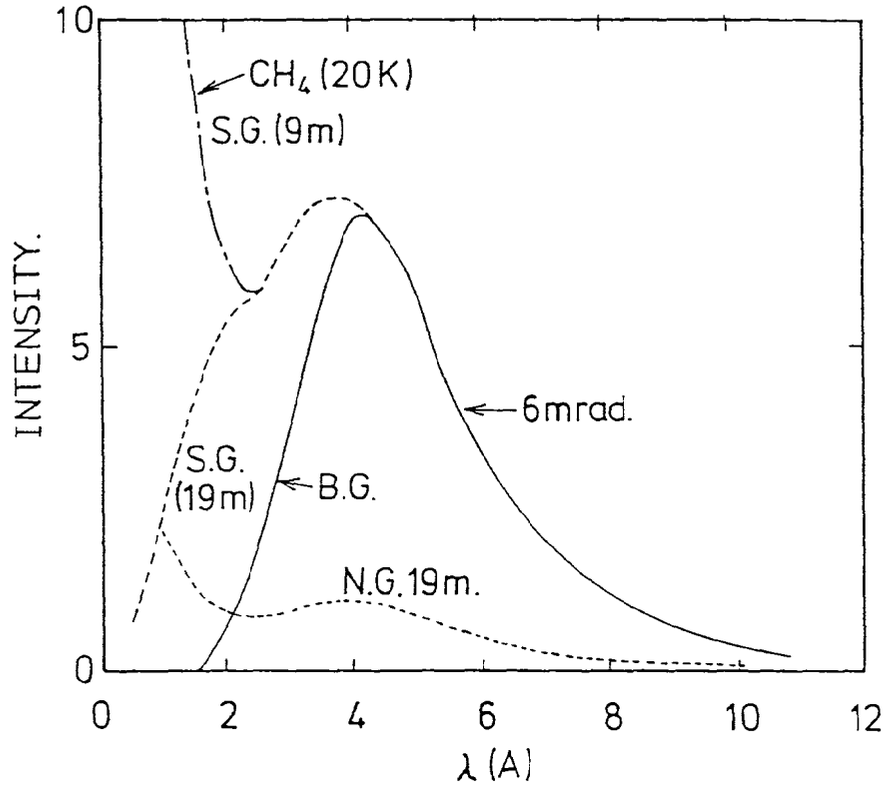
10
5
0
INTENSITY.
CH4 (20K)
S.G. (9m)
6mrad.
S.G.
(19m)
B.G.
N.G.19m.
0
2
4
6
8
10
12
λ (A)

Fig. 25

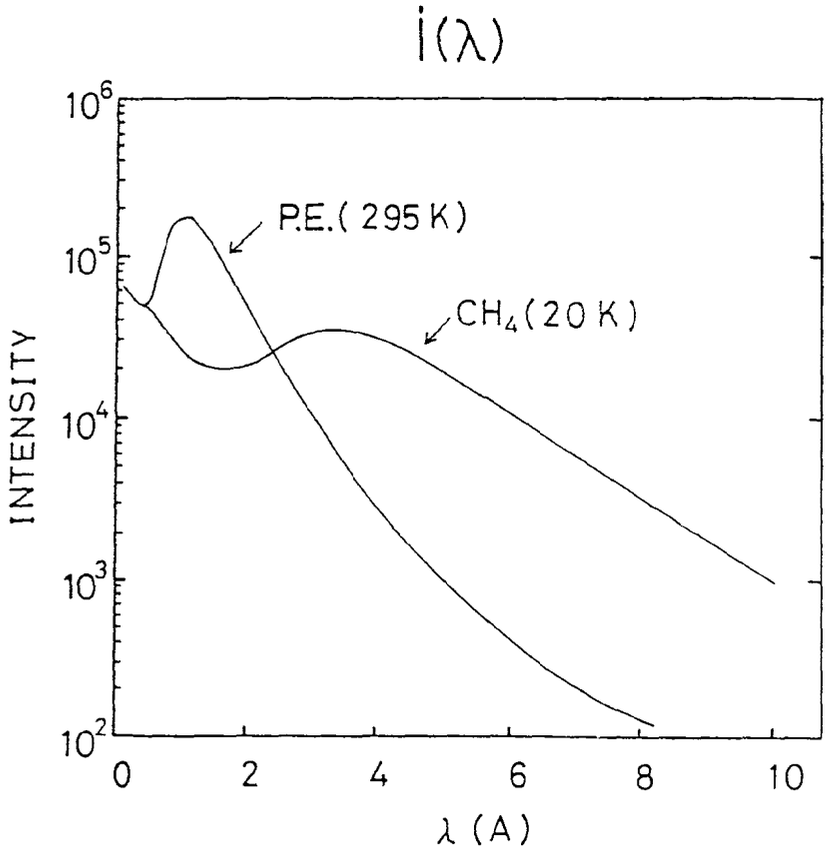
i(λ)
10^6
10^5
10^4
10^3
10^2
INTENSITY
P.E.(295 K)
CH4(20 K)
0
2
4
6
8
10
λ (A)

Fig. 23

GUIDE TUBE EFFICIENCY

(SAN)

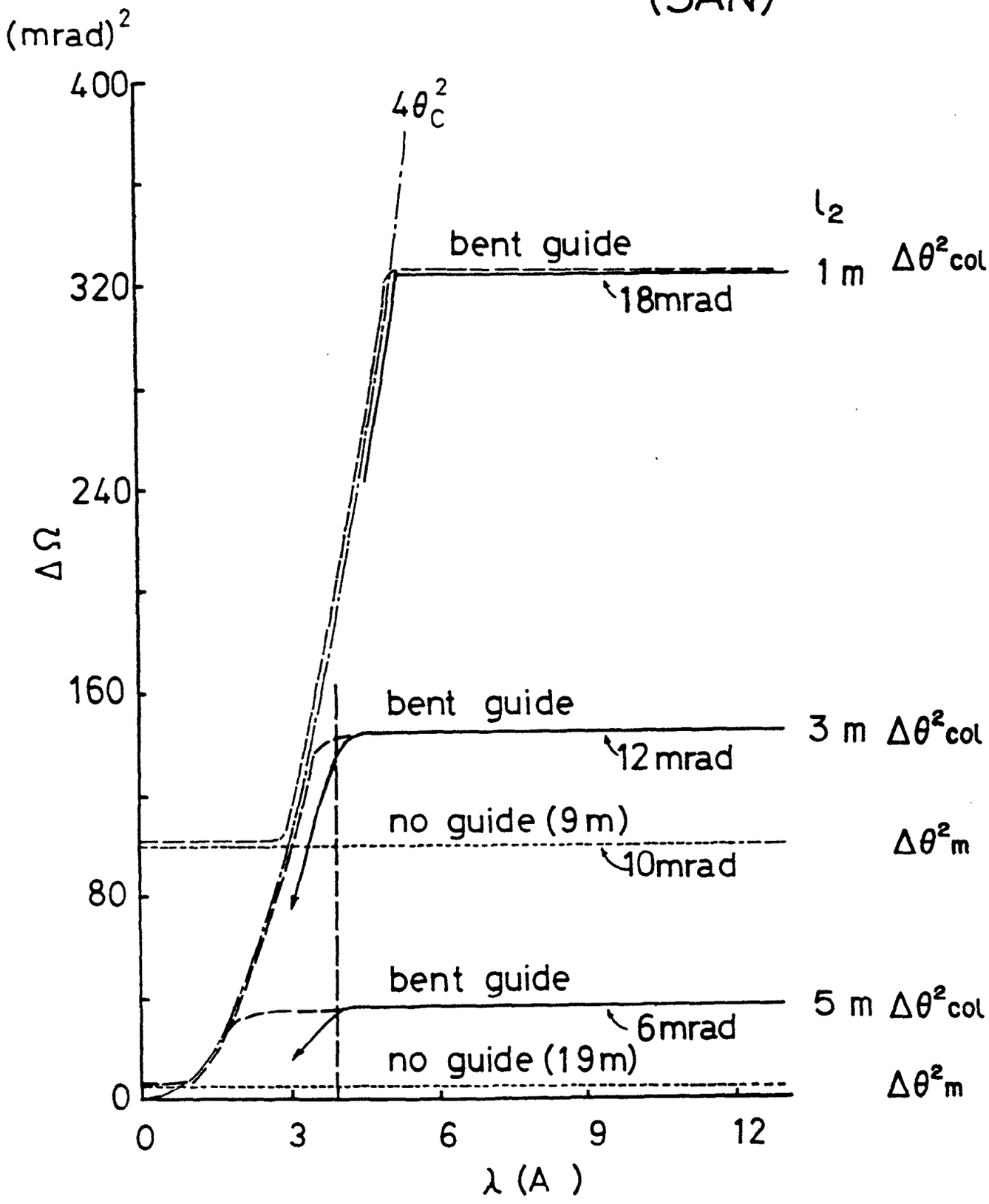

Fig. 24

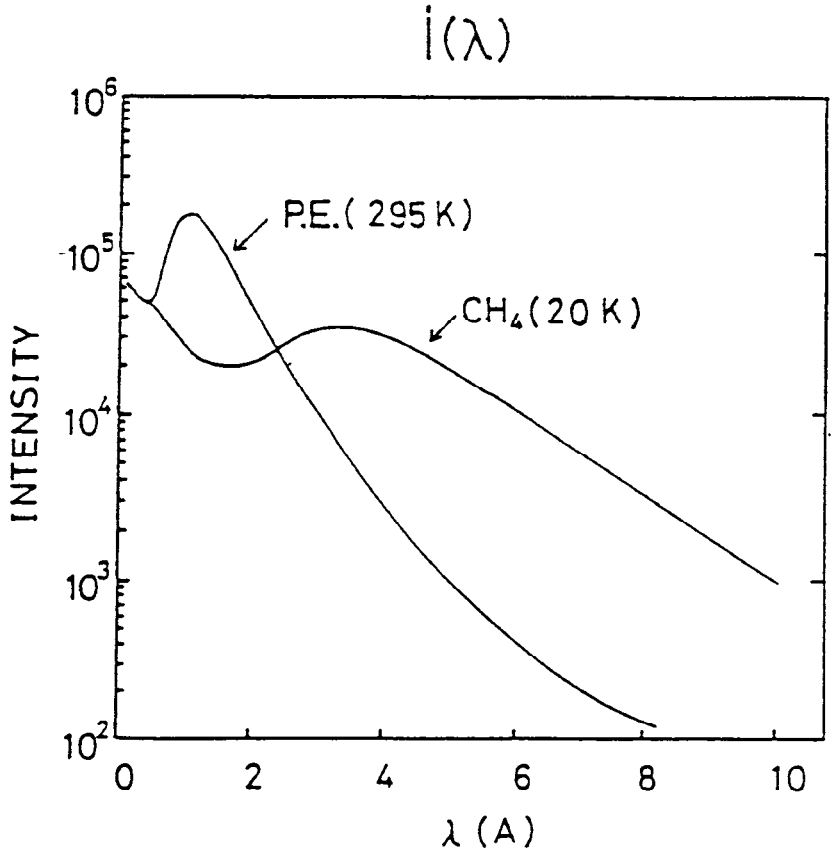
I(λ)
INTENSITY
10^6
10^5
10^4
10^3
10^2
P.E.(295 K)
CH4(20 K)
0
2
4
6
8
10
λ (A)

Fig. 23

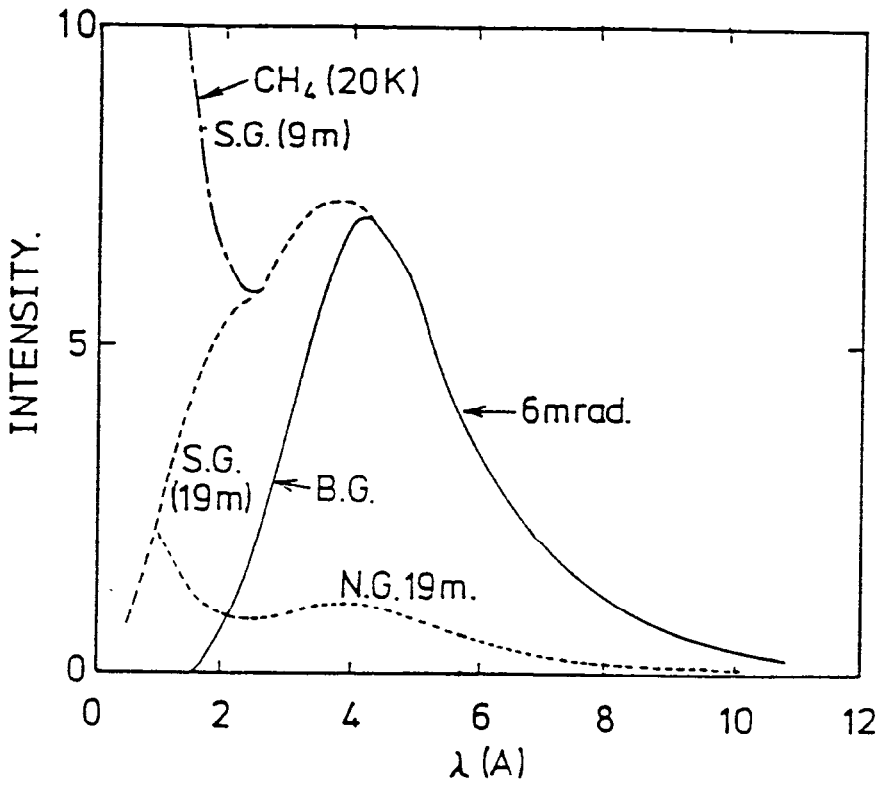
INTENSITY.
10
5
0
CH4 (20K)
S.G. (9m)
6mrad.
S.G.
(19m)
B.G.
N.G. 19m.
0
2
4
6
8
10
12
λ (A)

Fig. 25